

Phenomenon and processes involved in tyre-road friction

The main factor in tyre adherence is represented by the friction between the tyre tread and the road surface. Guiding further by the material presented by T. French in [1.1], the frictional force, F , has at least four components:

$$F = F_{\text{adhesion}} + F_{\text{deformation}} + F_{\text{viscous}} + F_{\text{tearing}}$$

The adhesion friction (F_{ad}) is the most significant component. It appears to have two factors: one is related to the molecular bonds between tread rubber and road; the other related to the shearing of the rubber just below the surface layer. The nature of the first factor is not completely clarified [1.1], [1.2], and [1.3]. Many specialists, like Kummer i.e., explain the adhesion as an electrostatic attractive force between the rubber molecules and the ions of the road surface. So, as a result of bonds formation and breaking, the rubber molecular chains encounter cyclic deformations that generate energy dissipation in sliding or rolling. Others, like Schallamach and Savkoor, explain the adhesion through Van der Waals forces. Beside this controversy, an important fact is that these forces are strongly dependent to sliding velocity and temperature (Figure 1).

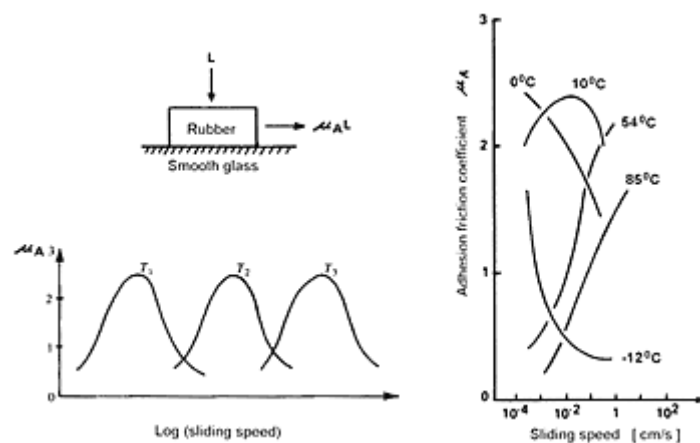


Figure 1 - Adhesion friction coefficient dependence to sliding speed and temperature. Adapted from [1.4]

In most practical cases, F_{ad} decreases as sliding velocity increases. It must be pointed that the WLF (Williams - Landel - Ferry) transform equation is very useful in the study of the adhesion friction.

The deformation friction (F_{def}) is significant when the tread rubber slides on a lubricated rough surface. As it could be seen in [figure 2](#), a layer of tread rubber that slides over a rough road encounters continuous deformations of compression and relaxation. On relaxation phase the rubber element returns only a part of the compression phase stored energy. The lost energy is converted in heat due to the rubber hysteresis phenomenon. So, appear a resistance force that is dependent to the hysteresis characteristic of the tread rubber and to the magnitude of deformation. Increasing the vertical load will increase the frictional force in a non-linear manner, so that the friction coefficient (friction force/normal load) would decrease. In addition, a greater contact area for a given load could imply a higher friction force.

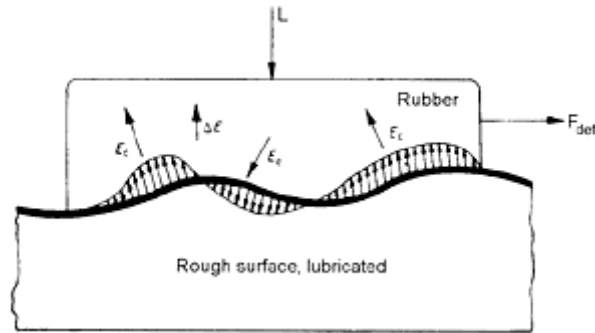


Figure 2 - The mechanism of deformation (hysteresis) friction

In the particular case of the heavy truck tyres, which must have a low hysteresis tread rubber in order to provide low heat generation and high tearing and cutting resistance, to obtain a high deformation friction remain a basic problem.

The viscous and tearing friction forces could appear to the specific tyre products and usages but in the most cases they are insignificant.

Normal and tangential stress distributions in the contact area

In the tyre loading and rolling processes due to the tyre deformations appear normal and tangential stresses in the contact area, stresses that affect the tyre adherence.

From the beginning it must be noticed that the value of nominal (net) contact area is smaller than the gross contact area due to tread design and somewhat due to the road roughness.

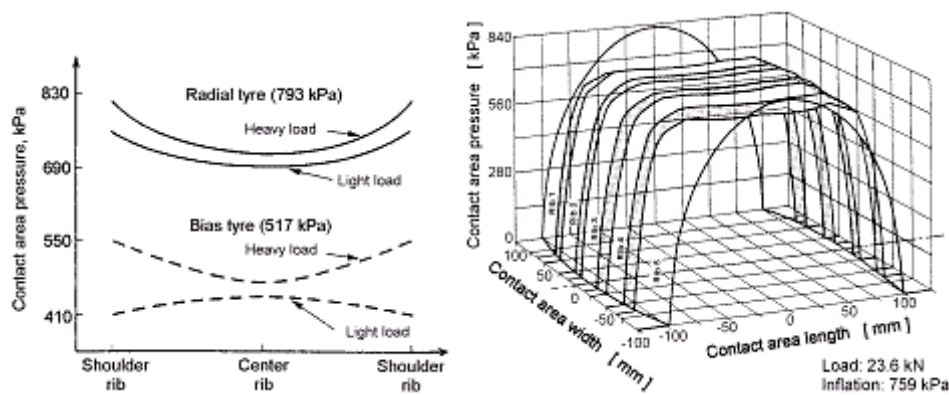


Figure 1 - Contact pressure of truck tyres [2.1]

Figure 2 - - Contact area pressure of 11R22.5 tyre [2.1]

The shape of the normal pressure variations measured across the middle of contact area to bias and radial truck tyres are presented in [figure 1](#) [2.1]. When the load increases in the bias tyre there is a greater transfer of load from the center to the shoulder. A typical normal pressure distribution in contact area obtained for a radial truck tyre is shown in [figure 2](#).

Because the normal pressure is not constant on the contact area, the friction force varies from point to point. Also, the tangential stresses encountered in contact area ([figure 3](#)) due to tyre deformation could generate slip (slide) movements affecting adherence. The displacement of tread elements along the tyre contact area during free rolling, driving and braking are presented in [figure 4](#).

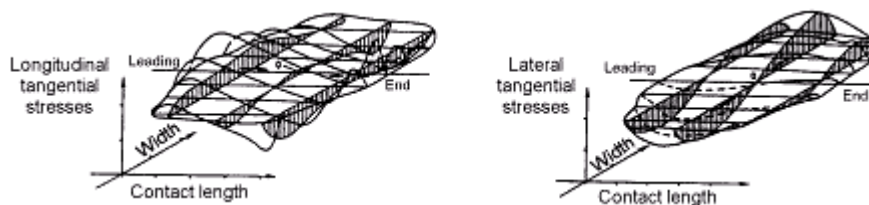


Figure 3 - Tangential stresses distribution in contact area of free rolling tyre [2.2]

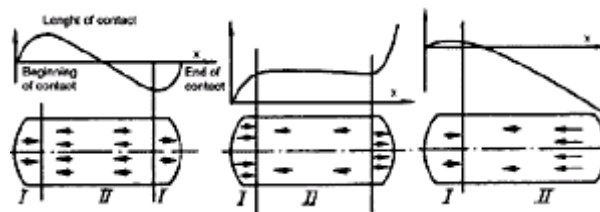


Figure 4 - Displacement of tread elements along the tyre contact area length [2.3]

Tyre-road friction and tyre slip

Let us consider the truck-tyre in detail.

When braking the tyre in stationary conditions, the normal force acts just in front of the wheel centre. Within the contact area a shear stress arises that increases until the adhesion limit is reached and sliding occurs, after which it decreases broadly proportional (Coulomb friction assumed) with the locally occurring normal stress.

The speed of the tyre relative to the wheel centre first increases. When the adhesion limit is reached, a sliding speed arises locally, resulting in a nonzero average speed V_{slip} of the rubber within the contact area. The ratio of this speed and the wheel speed in percent is designated the longitudinal slip $s_x = -$

κ :

$$s_x = \kappa = \frac{V_{slip}}{V} = \frac{V - \omega \cdot R_e}{V} [\%]$$

If a side force operates on the tyre, a lateral deformation appears in the tyre belt and its tread. Points on the running surface experience the belt deformation before they make contact with the road at which point the tyre first attempts to maintain contact with the road surface.

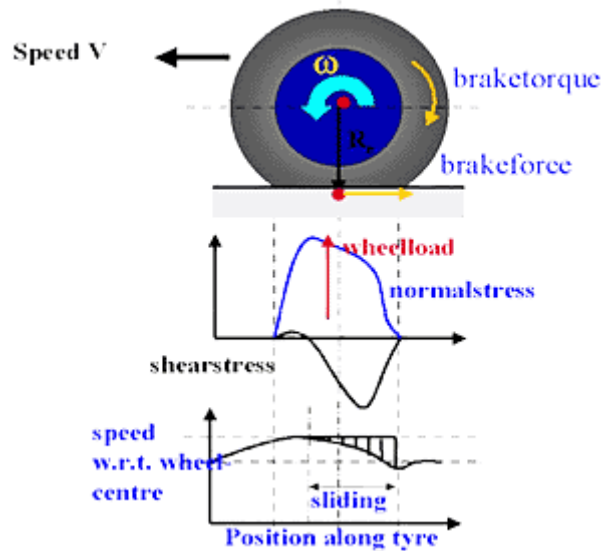


Figure 1 - Braking the tyre

This corresponds to a gradually increasing shear stress in lateral direction. Once the adhesion limits are reached, the rubber will start to slide relative to the road with a lateral motion, perpendicular to the wheel plane. The asymmetry in the distribution of shear stress causes the resulting force not to grip exactly in the middle of the contact area just under the wheel centre. Rather there is a pneumatic trail which, in combination with the side force, produces an aligning torque which tries to push the tyre in the direction of the wheel speed. The tangent of the slip angle between wheelplane and wheel speed, denoted as side slip $-s_y$:

$$s_y = \tan(\alpha)$$

in conjunction with the wheel load and the camber angle, are decisive for the side force and the aligning torque.

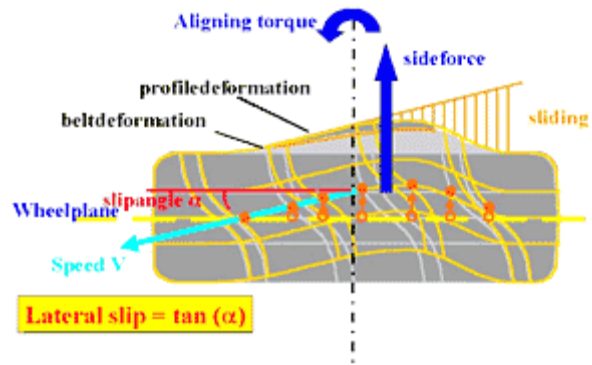


Figure 2 - Cornering of a tyre

The relationships between the position of the tyre, in terms of the slip values, and tyre response in terms of longitudinal and lateral force, pneumatic trail and aligning torque are of essential importance in studying vehicle behaviour. Without a good description of these tyre characteristics, such kind of research is impossible.

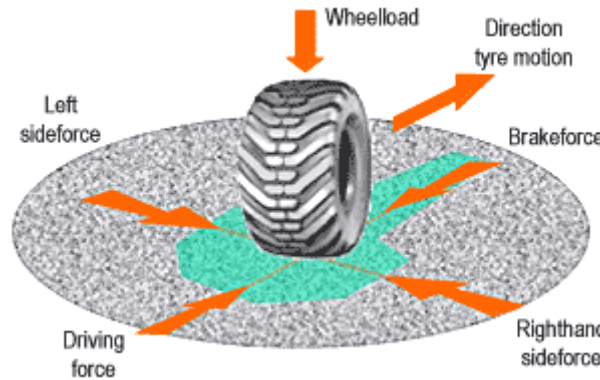


Figure 3 - A tyre under combined slip conditions

Besides the properties described in pure slip conditions, one is also interested in situations of combined slip which are pertinent to braking when cornering. The maximum shear force between tyre and road surface is given by the existent coefficient of friction multiplied by the wheel load. The implication for braking in a bend is that the possible maximum brake force relative to a situation of straight line braking will be reduced. One has therefore sacrificed braking potential which is indicated by the friction ellipse, in which realistic combinations of brake or drive force and side force are shown separately.

Tyre characteristics

The above discussion finally leads to relationships between:

- Side force versus lateral slip
- Pneumatic trail versus lateral slip
- Aligning torque versus lateral slip
- Brake or drive force versus longitudinal slip

under pure slip conditions (only lateral or longitudinal slip). In case of combined slip, the side force also depends on longitudinal slip, etc. Typical examples of these pure slip characteristics are shown in [figure 4](#). One observes a strong nonlinear behaviour for larger slip. These relationships are of essential importance in studying vehicle behaviour. Without a good

description of these tyre characteristics, such kind of research is impossible. The slope of the side force F_y vs. slip angle α near $\alpha = 0$ (the cornering stiffness) is the determining parameter in the linear basic handling and stability theory of automobiles, as we shall see later.

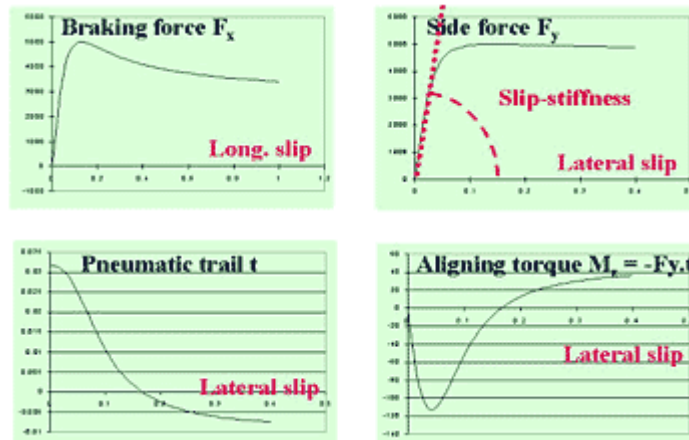


Figure 4 - Some typical tyre characteristics

Under combined slip conditions, typical plots of F_x (brake or drive force) versus F_y (cornering force) are shown below for fixed values of slip angle α (taken from DELFT-TYRE). For small values of α , the side force almost vanishes. As α increases, the side force F_y becomes apparent at the cost of a lower maximum value of the longitudinal force F_x .

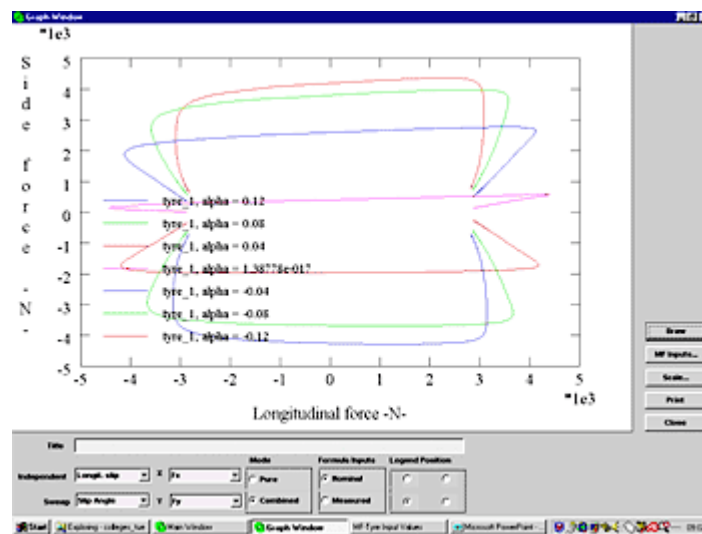


Figure 5 - Combined slip, F_x versus F_y

It is important to note that tyre shear forces depend on tyre load. This dependence is usually nonlinear, where for increasing tyre load, the absolute slope of the tyre force versus tyre load reduces. This is the reason why during cornering, the average lateral tyre force per axle reduces due to force redistribution from inner to outer wheel. Consequently, as we shall see later, the steering performance of the vehicle is changed which might even lead to yaw-instability (oversteer conditions).

An example is shown in [figure 6](#) with F_y depicted vs. load F_z for three different slip angle. One observes the decreasing absolute slope of these curves,

meaning that under load transfer of for example 1500 N (being the increase, decrease of the tyre load at outer and inner tyre, respectively) and with an axle slip angle of 0.08 rad., the total lateral force is reduced. In other words, the cornering stiffness is reduced due to this load transfer.

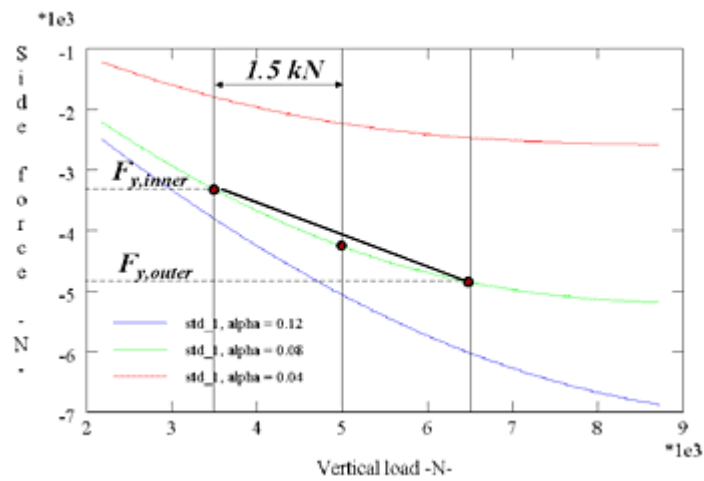


Figure 6 - Load sensitivity lateral force

The illustration is for passenger cars, for which a restricted load variation is apparent. This is different for truck tyres where large variations in payload and thus large variations in tyre load will occur. This is illustrated in [figure 7](#) where the normalized cornering stiffnesses (cornering stiffness coefficient: tyre cornering stiffness divided by the tyre load) for typical truck and passenger car tyres are depicted vs, tyre load. One observes a decreasing trend for both passenger and truck tyres, with a much smaller sensitivity for truck tyres compared to passenger tyres.

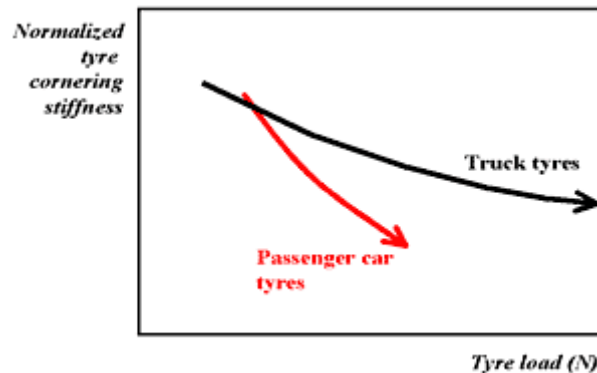


Figure 7 - Load sensitivity passenger car and truck tyres

We close this section with some remarks concerning factors that influence tyre characteristic curves. The variations of the longitudinal force coefficient (defined as F_x/F_z) and longitudinal force versus longitudinal slip of two truck radial tyres are depicted in [figure 8](#) and [figure 9](#). The peak value is the maximum that can be reached without wheel locking, while the slide value is obtained during the locked wheel. [Figure 10](#) presents some typical ranges of values of the longitudinal force coefficient obtained on a dry concrete surface for bias and radial tyres with two type of tread patterns design.

The dependencies of the longitudinal force coefficient to the load and speed

are presented in [figure 11](#) and [figure 12](#).

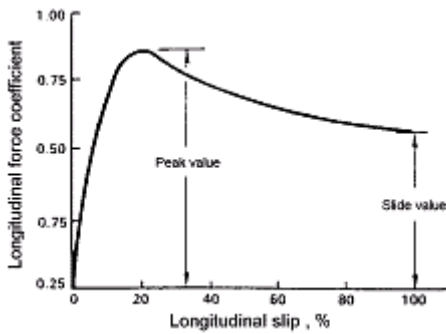


Figure 8 - Longitudinal force coefficient vs. slip

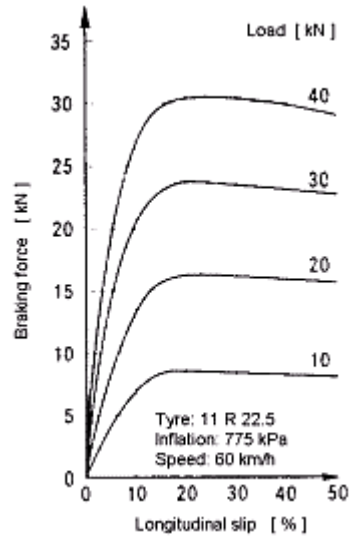


Figure 9 - Braking force vs. slip of a truck tyre [3.1]

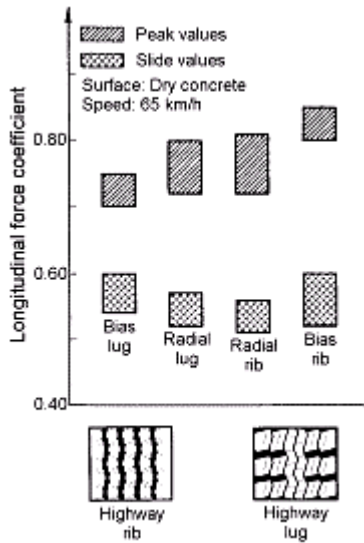


Figure 10 - Longitudinal force coefficient on dry road [2.1]

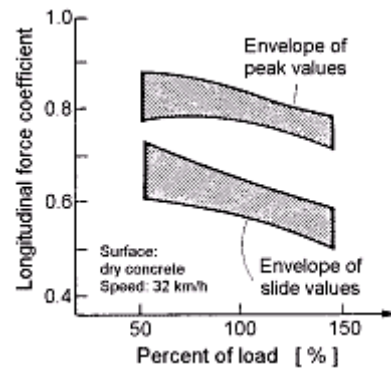


Figure 11 - Effect of load (radial tyre) [2.1]

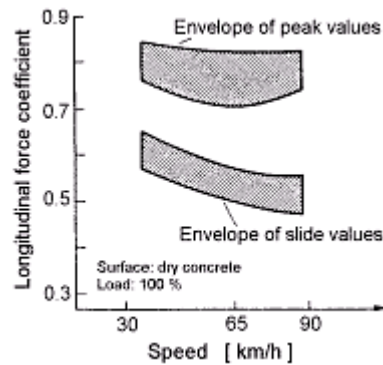


Figure 12 - Effect of speed (radial tyre) [2.1]

Next, we consider the lateral force in more detail. This force is a function not only of simple friction but also of the size, design, construction and operating

condition (i.e. load and inflation pressure).

The influences of the tyre construction and loading condition to lateral force coefficient (defined as F_y/F_z) are presented in [figure 13](#) and [figure 14](#).

It must be noticed that radial truck tyres are more responsive than bias truck tyres and the low profile radial truck tyre has a more constant lateral force coefficient through the load change (important in suspension design).

Combining braking and cornering by adding braking force to a tyre which rolls with slip angle results the friction ellipse concept. This ellipse envelops all the plotted curves of lateral forces versus longitudinal forces for different slip angles, as discussed above. [Figure 15](#) and [figure 16](#) show some combined forces for two truck tyres (bias and radial) while [figure 17](#) shows the influence of slip angle on braking forces.

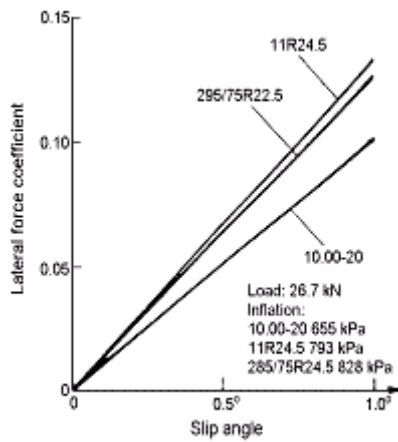


Figure 13 - Effect of tyre construction [2.1]

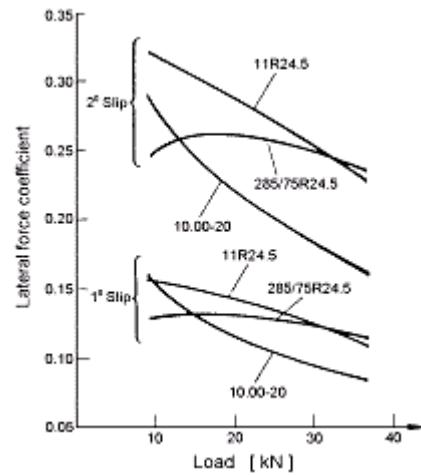


Figure 14 - Effect of load [2.1]

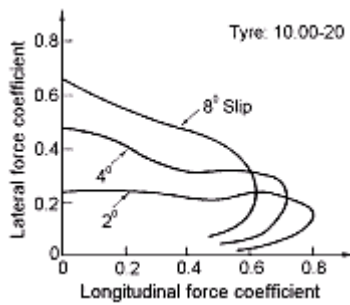


Figure 15 - Braking and cornering (bias tyre) [2.1]

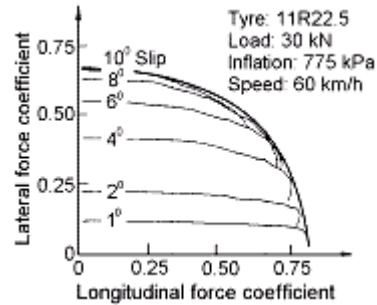


Figure 16 - Braking and cornering (radial tyre) [3.1]

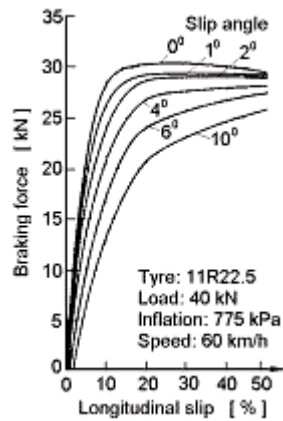


Figure 17 - Influence of slip angle on braking forces [8]

Adherence under special road conditions

The road surface conditions and temperature are important for the adherence values. In real conditions the road could be contaminated with dust, mud or sand, or covered with water, ice or snow.

On the wet roads, when the water thickness is very low and motor vehicle speed in normal range, it could be observed a somewhat decrease of adherence. This fact could be explain due to the diminish value of adhesion friction on lubricated surfaces. The peak and slide values of the longitudinal force coefficient on wet road compared to the values on dry road are presented in [figure 1](#).

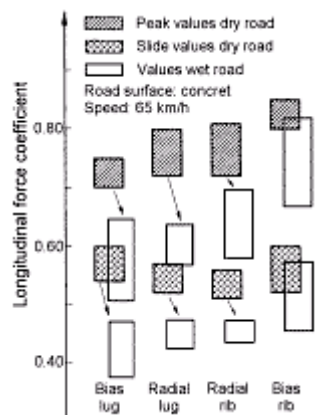


Figure 1 - Compare between dry and wet road adherence conditions, adapted from [1]

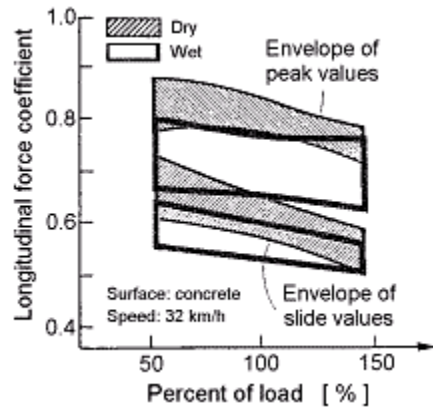


Figure 2 - Compare of load effect on dry and wet roads (radial truck tyre), adapted from [1]

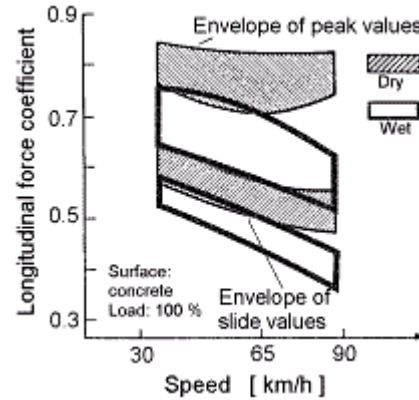


Figure 3 - Compare of speed effect on dry and wet roads (radial truck tyre), adapted from [1]

In addition, the influences of load and vehicle speed are depicted in [figure 2](#) and [figure 3](#).

When the water layer thickness and vehicle speed increase the hydroplaning phenomenon appear. So, the tyre is lifting from the road surface due to the pressure created by water under tyre. The tyre behavior between the state in which hydroplaning begin and the full (total) hydroplaning state, is commonly described with the "three-zone concept" elaborated by Dr. V.E. Gough in 1959. As can be seen in [figure 4](#), zone A (unbroken water film) is in forward region of the contact area where the hydrodynamic pressure lifts and completely separates the tread from the road. In this region the water film remains unbroken and the local coefficient of friction is substantially zero. Zone B (transition zone) is the region where a progressive breakdown of the water is dissipated but where a thin film layer of water still remains. In this region the effective coefficient of friction varies widely. Zone C ("dry" contact) is the region where the lubrication film has been substantially removed and the road frictional forces can be generated. The image of contact area of a heavy truck tyre that rolls on a smooth glass surface covered with water is shown in [figure 5](#).

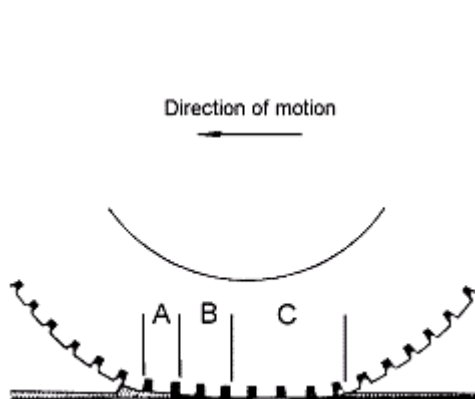


Figure 4 - The three-zone concept of contact area

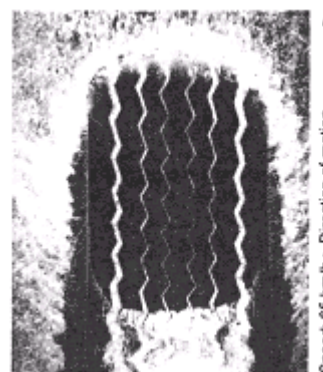


Figure 5 - Contact area of a truck tyre rolling through a film of water [5]

The key objective in order to improve the adherence in this case is to increase the length of zone C through an optimum tread pattern design.

The percent of hydroplaning is given by the equation:

$$\text{Hydroplaning} = \frac{\text{Dynamic contact area}}{\text{Static contact area}} \times 100$$

The magnitude of hydroplaning is affected by:

- water conditions - water depth, surface texture and drainage;
- pressure distribution in contact area - construction, size, tread shape, worn;
- tyre patterns design - groove capacity on removing water.

Considering the studies about the effects of the rain, which states that the water depths on an well-drain road are generally less than 1 mm and could reach values of 1 to 2 mm in the first five minutes of thunder showers, the most hydroplaning tests are done with a water depth of 2 mm [2.1].

The effects of tyre construction (bias and radial), speed, tread design and tread wear on hydroplaning are presented in [figure 6](#), [figure 7](#) and [figure 8](#).

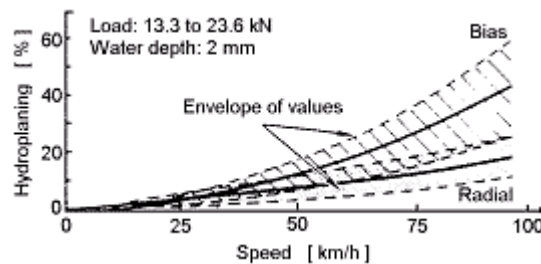


[Figure 6](#) - Effect of tyre construction on hydroplaning [1]

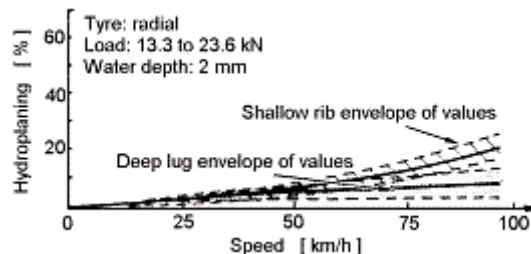


[Figure 7](#) - Effect of tread design on hydroplaning [1]

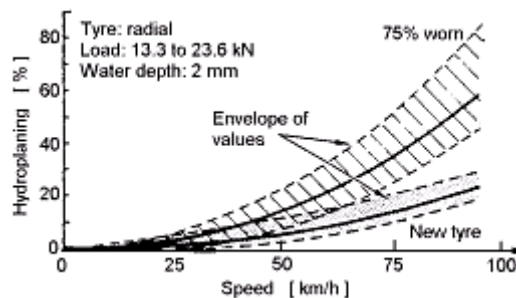


[Figure 8](#) - Effect of treadware on hydroplaning [1]

Analyzing the figures it can be observed that the radial heavy truck tyre construction offers improved hydroplaning resistance. Also, almost 2.5 times

improved performances (at speed of 90 km/h) are encountered by the deeper tractive lug pattern design compared to shallow rib design and by new tyre compared to 75 % worn tyre.

The adherence on road covered with snow is greatly dependent by factors like:

- tread pattern geometry;
- lateral sipe density;
- rubber-to-void ratio;
- tread compound.

The relative effect of the tread design of a truck tyre to adherence, tested on a surface of 5-10 mm of loose snow implies in 1.3 - 1.8 times improved longitudinal force for radial lug design compared to radial rib design.

Finally, an adherence performance analysis of a large truck tyre rolling on a dry, wet and snow-packed road surface is illustrated in [figure 9](#), [figure 10](#) and [figure 11](#) [3.1].

While on dry and wet road surfaces the maximum lateral forces appear in slip angle domains above 10° , correspondingly smaller maximum lateral forces are attained already at slip angle of 5° to 7° on snow-packed road surfaces due to the lower coefficient of friction. For braking forces the maximum on a dry asphalt road appears in the range of 20% slip, on wet road are already evident at 15 % slip and on snow-packed roads at 8% already. As the friction between tyre and road decreases, the load dependence decreases also. It must be noticed that on the maximum coefficient of adherence of snow-packed roads the surface temperature has a pronounced influence.

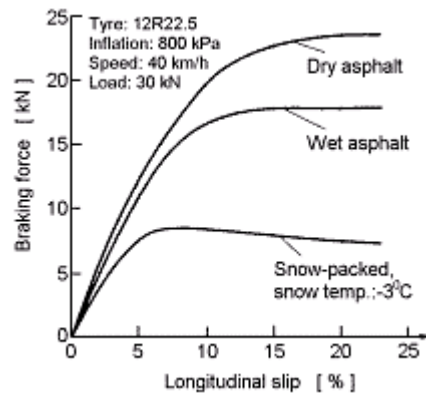


Figure 9 - Braking forces on different road surfaces [4]

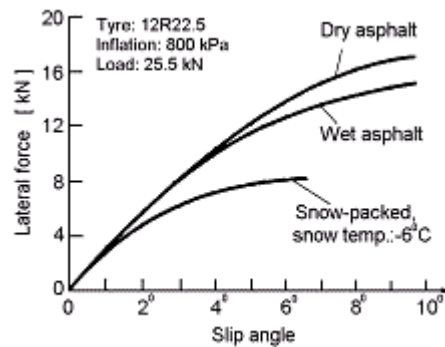


Figure 10 - Lateral forces on different road surfaces [4]

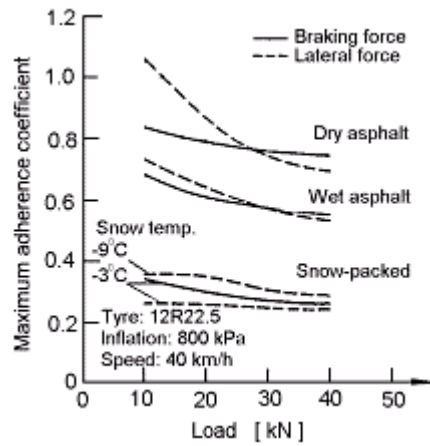


Figure 11 - Maximum adherence coefficient for braking and lateral forces on different road surfaces [4]

The single track vehicle model

Some attention will be paid to the more fundamental aspects of possible truck motions and we start with a single truck. This part of the document deals with rather straight forward vehicle dynamics and details can be found for example in [5.1], [5.2] and [5.3]. We'll treat this in some detail to clarify the role of the tyre characteristics in vehicle response, and take the simplest possible automobile model which runs at constant speed over an even horizontal road surface.

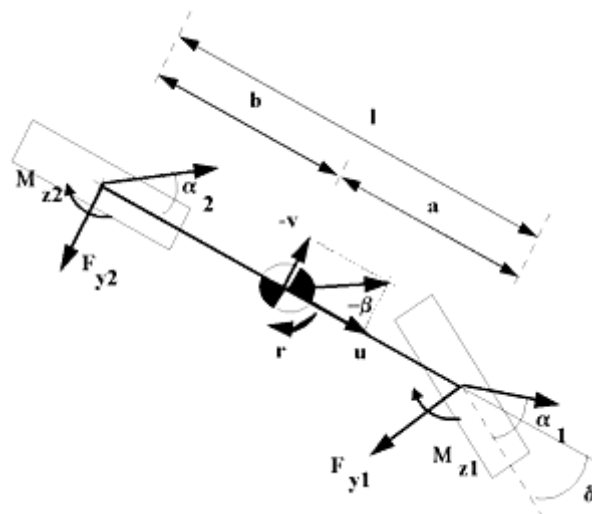


Figure 1 - Simple one-track vehicle model

The steer and slip angles are restricted to relatively small values. The driving

force required to keep the speed constant is assumed to remain small with respect to the lateral forces acting on the tyre. Brakeforces will be neglected as well for the time being.

In addition, it is assumed that small friction coefficients exist between tyre and road, or the centre of gravity of the vehicle is low relative to the track width. That means that body roll and pitch behaviour can be neglected. It also means that load transfer between front- and rear axle is neglected. With these assumptions, the front wheels can be taken as one system, with an overall lateral force, aligning torque, slip angle obtained from the combined effect of left and right wheel. A similar simplification holds for the rear wheels. That means that tyre characteristics are replaced by axle characteristics. Load transfer between left and right wheels can be taken into account by adjustment of the axle characteristics. For the time being, special axle configurations (dual tyres, two- and three axle combinations) will be described as one axle, with adjusted lateral axle configurations and vehicle parameters in an appropriate way. This finally leads to a vehicle model as shown in [figure 1](#). For trucks with such multiple non-steering axles and/or dual tyres, it was observed by Winkler in [5.8] that a simplified model still holds for an equivalent increased wheel-base. More specific, the axle configurations as mentioned effect the steering axle on top of the influence of the lateral acceleration. In other words, the necessary steering angle to negotiate a curve is not only depending on the lateral acceleration a_y but also on the radius of curvature, independent of a_y .

Both in the linear case (linear tyres) as in the case of nonlinear load dependency of the tyre lateral characteristics, this can be accounting for (exact for linear tyres, a good approximation for the nonlinear load dependency) by shifting the front axle more to the front, and the rear axle-configuration slightly further to the rear. We shall come back to this in more detail, further on in this section.

The slip angles for the front and rear axle are denoted by α_1 and α_2 . The total lateral force and aligning torque for front and rear axle are denoted by F_{y1} and F_{y2} , and M_{z1} and M_{z2} , respectively. The aligning torques will be disregarded in the forthcoming analysis. The vehicle centre of gravity (c.o.g.) is positioned between both axles, at distances a and b from front and rear axle, respectively. The horizontal behaviour of the vehicle is described by a lateral velocity v at the c.o.g., a forward velocity u , a yaw rate r and a bodyslip angle β . This bodyslip angle follows from:

$$\beta = \arctan\left(\frac{v}{u}\right) \approx \frac{v}{u} \quad (\text{Eq 1})$$

for small lateral velocity v . The equations of motion follow from the statements that equilibrium must hold in lateral and yaw direction. The lateral vehicle acceleration must be balanced by the lateral tyre forces. The yaw moment acting on the vehicle must be balanced by the moment due to the tyre forces (where aligning torques are neglected). This leads to the following equations:

$$m(\dot{v} + u \cdot r) = F_{y1} + F_{y2}$$

$$J_z \dot{r} = a \cdot F_{y1} - b \cdot F_{y2} \quad (\text{Eq 2})$$

with vehicle mass m , and J_z the polar moment of inertia in z -direction (yaw moment of inertia). To be more accurate, the pneumatic trails front and aft should have been accounted for in the second equation of

(Eq 2) but these effects will be disregarded. The axle loads front and aft follow from equilibrium in the xz-plane:

$$F_{z1} = m \cdot g \cdot \frac{b}{a+b} = m \cdot g \cdot \frac{b}{l}; \quad F_{z2} = m \cdot g \cdot \frac{a}{a+b} = m \cdot g \cdot \frac{a}{l} \quad (\text{Eq 3})$$

with acceleration of gravity g and wheelbase l . It is sometimes convenient to approximate the yaw moment of inertia by the value obtained with all mass concentrated at front and rear axle:

$$J_z \approx J_{z,conc.} = a^2 \cdot \frac{mb}{l} + b^2 \cdot \frac{ma}{l} = m \cdot ab \quad (\text{Eq 4})$$

The set of equations (Eq 2) is formulated in terms of two dependent variables, v and r . The lateral axle forces F_{y1} and F_{y2} depend on the slip angles α_1 and α_2 :

$$F_{y1} = F_{y1}(\alpha_1) \quad \text{and} \quad F_{y2} = F_{y2}(\alpha_2) \quad (\text{Eq 5})$$

where we recall that these functions are highly nonlinear in slip angle (see figure 4 in chapter "Tyre-road friction and tyre slip") where tyre forces are depicted. These slip angles depend on v and r through:

$$\alpha_1 = \delta - \frac{v+ar}{u}; \quad \alpha_2 = -\frac{v-br}{u} \quad (\text{Eq 6})$$

with steering angle δ . That means that the state variables v and r can be replaced by the slip angles α_1 and α_2 , resulting with the approximation $J_z = m \cdot ab$ in:

$$\begin{pmatrix} \dot{\alpha}_1 \\ \dot{\alpha}_2 \end{pmatrix} = \frac{u}{l} \cdot (\alpha_2 - \alpha_1 + \delta) \begin{pmatrix} 1 \\ 1 \end{pmatrix} - \frac{g}{u} \cdot \begin{pmatrix} f_{y1} \\ f_{y2} \end{pmatrix} + \begin{pmatrix} \dot{\delta} \\ 0 \end{pmatrix} \quad (\text{Eq 7})$$

with the normalized lateral axle-forces defined by:

$$f_{y1}(\alpha_1) = \frac{F_{y1}(\alpha_1)}{F_{z1}}; \quad f_{y2}(\alpha_2) = \frac{F_{y2}(\alpha_2)}{F_{z2}} \quad (\text{Eq 8})$$

The lateral forces can be taken in its full nonlinear setting (in slip angle), or they may be approximated by linear relationships $C_{F_{oi}} \cdot \alpha$ with cornering stiffness $C_{F_{oi}}$ for front and rear axle (with $i=1, 2$, respectively) in case of small slip angle α , see figures 4 and 13 in chapter "Tyre-road friction and tyre slip" and figure 10 in chapter "Adherence under special road conditions". For smaller cars like vans, pick-up trucks, this nonlinear behaviour in the slip angle is important. For larger commercial vehicles, tyres are usually used in the linear range of slip angles, but the load dependency (also being nonlinear) plays a more dominant role here, see also figure 6 and figure 7 in chapter "Tyre-road friction and tyre slip". Knowing this load sensitivity (from tyre tests), one can determine axle cornering force vs. slip angle characteristics, with these effects taken into account. Both type of nonlinearities will be discussed.

The reader should be aware of these different types:

1. nonlinear load dependency, to be accounted for by equivalent axle- and vehicle parameters
2. nonlinearity in slip angle, relating to the lateral tyre behaviour under excessive side-slip.

Note that cornering stiffness refers to the axle characteristics. Expressing the right-hand side of (Eq 2) in terms of the tyre cornering stiffness, a factor has to be included being 2 if load transfer is not taking into account (else it would be less than 2).

Introduce the cornering stiffness coefficients C_0 , C_1 and C_2 by:

$$\begin{aligned} C_0 &= C_{Fx1} + C_{Fx2} \\ C_1 &= a.C_{Fx1} - b.C_{Fx2} \\ C_2 &= a^2.C_{Fx1} + b^2.C_{Fx2} \quad \text{(Eq 9)} \end{aligned}$$

Then, system (Eq 2) in combination with (Eq 6) assuming linear tyre behaviour simplifies to:

$$\begin{aligned} m \cdot \frac{C_0}{u} \cdot v + (mu + \frac{C_1}{u}) \cdot r &= C_{Fx1} \cdot \delta \\ J_z \cdot \frac{C_1}{u} \cdot v + \frac{C_2}{u} \cdot r &= a.C_{Fx1} \cdot \delta \quad \text{(Eq 10)} \end{aligned}$$

We'll continue to discuss the steady state solutions of (Eq 2). That means that we consider vehicle behaviour as described by the steady state circular test, ISO 4138. These steady state solutions correspond to the singular points for the full dynamic system.

Under steady state conditions, time derivatives vanish and (Eq 2) reduces to:

$$\begin{aligned} m \cdot u \cdot r &= F_{y1} + F_{y2} \equiv K \\ a \cdot F_{y1} &= b \cdot F_{y2} \quad \text{(Eq 11)} \end{aligned}$$

with total centrifugal force $K=m \cdot u \cdot r$. In terms of the axle loads as given by (Eq 3), one finds:

$$\frac{F_{y1}(\alpha_1)}{F_{z1}} = \frac{F_{y2}(\alpha_2)}{F_{z2}} = \frac{u \cdot r}{g} = \frac{u^2}{gR} = \frac{K}{mg} \quad (=a_y \text{ in } g's) \quad \text{(Eq 12)}$$

for radius of vehicle path R .

Hence, the normalized axle characteristics front and aft coincide:

$$f_{y1}(\alpha_1) = f_{y2}(\alpha_2) \quad \text{(Eq 13)}$$

The lateral acceleration K/mg depends on the relative path curvature l/R in a linear sense:

$$\frac{K}{mg} = \frac{u.r}{g} = \frac{u^2}{g.l} \cdot \frac{l}{R} \quad (\text{Eq 14})$$

In terms of this same relative path curvature, it follows from the relationships (Eq 6) between slip angles and state variables (v,r) that:

$$\delta - \alpha_1 + \alpha_2 = \frac{r.l}{u} = \frac{l}{R} \quad (\text{Eq 15})$$

Note that different sets of (α_1, α_2) may satisfy (Eq 13) and (Eq 15) due to the nonlinear behaviour of f_{y1} and f_{y2} . This has been illustrated in [figure 2](#), where two normalized tyre curves are shown. One is looking for sets (α_1, α_2) , with a difference equal to $\delta - l/R$ and with equal values of f_{yi} . Two pairs of solutions are indicated, one corresponding to both the parts of both curves with positive slope, and one corresponding to part of f_{y1} where the slope is negative ('over the top').

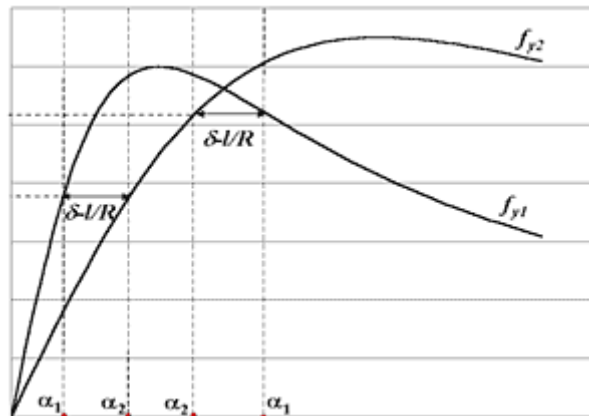


Figure 2 - Different steady state solutions

Summarizing, one observes from the previous expressions that the centrifugal force K can be described in terms of both the slip angles through the normalized tyre curves (these relationships being highly nonlinear) and in terms of the path curvature where slip angles and path curvature are related through (Eq 15).

Let us examine (Eq 12) and (Eq 15) in more detail, and we start with linear tyre behaviour. Then one finds from (Eq 12) that:

$$\frac{u^2}{g.R} = \frac{C_{Fz1} \cdot \alpha_1}{F_{z1}} = \frac{C_{Fz2} \cdot \alpha_2}{F_{z2}}$$

That means that:

$$\left[\frac{F_{z1}}{C_{Fz1}} - \frac{F_{z2}}{C_{Fz2}} \right] \frac{u^2}{g \cdot R} \equiv \eta \cdot \frac{u^2}{g \cdot R} = \eta \cdot a_y(g) = \alpha_1 - \alpha_2 = \delta - \frac{l}{R} \quad (\text{Eq 16})$$

with coefficient η , referred to as understeer gradient.

This relationship expresses clearly the dependency of the vehicle cornering performance on tyre characteristics. This can be explained as follows.

For very low speed u , the steering angle in order to negotiate a curve is equal to the relative curvature l/R (Ackermann angle). Driving faster over the same curve (circle with radius R), the necessary change in required steering angle depends on the understeer gradient and hence on the tyre characteristics. For positive understeer gradient η , the steering angle δ has to increase whereas for negative value of η , the opposite is true and the steering angle δ has to be reduced. In the second case, without this change in δ , the vehicle would end up on a curve with a smaller curve radius. In other words, increasing speed leading to larger lateral acceleration and hence more extreme conditions, at the same time leads to a smaller curve radius increasing further the lateral acceleration, without corrective action by the driver. It will be demonstrated in subsequent sections that, beyond a certain speed, this case will lead to instability.

It was mentioned by Winkler in [5.8], as an extension of the work of Pacejka [5.5 - 5.7], that for a truck with multiple non-steering axles and possibly duals tyres, expression (Eq 16) should be replaced by:

$$\delta - \frac{l}{R} = \eta \cdot a_y(g) + \frac{1}{l \cdot R} \left[\frac{\sum_{i=1}^N \Delta_i^2}{N} + D^2 \cdot \frac{C_{s2}}{C_{Fz2}} \right] \left(1 + \frac{C_{Fz2}}{C_{Fz1}} \right) \quad (\text{Eq 17})$$

with longitudinal distance Δ_i from the aft end of the average position of the rear axle configuration to the i^{th} axle, C_{s2} the sum of longitudinal stiffnesses of all rear tyres, and D the lateral spacing between the dual tyres. Assuming the influence of dual tyres to be small compared to multiple axles, and introducing the tandem factor T by:

$$T = \frac{1}{N} \sum_{i=1}^N \Delta_i^2 \quad (\text{Eq 18})$$

one arrives at (for linear tyres):

$$\delta - \frac{l}{R} = \eta \cdot a_y(g) + \frac{T}{l \cdot R} \left(1 + \frac{C_{Fz2}}{C_{Fz1}} \right) \quad (\text{Eq 19})$$

Observe that the deviation of the steering angle from the Ackermann-value now not only depends on a_y but also on the curvature l/R . This expression can be rewritten in the form (Eq 16) by replacing the wheel base l by an equivalent wheel base l_e :

$$l_e = l \left[1 + \frac{T}{l^2} \left(1 + \frac{C_{Fz2}}{C_{Fz1}} \right) \right] \quad (\text{Eq 20})$$

A similar kind of expression for an equivalent wheel base can be derived (according to [5.8]) in case of nonlinear dependency on tyre load. One then arrives at an expression which approximately coincides with (Eq 16). In the remaining part of this document, we shall write l instead of l_e , where one should realize that the results hold for trucks with complex axle configurations by applying (Eq 20).

As one observes from (Eq 16), the understeer gradient is written as the difference of two terms, related to the front axle and the rear axle. These two terms are denoted as cornering compliance of the front axle, CC_f and rear axle, CC_r , respectively.

Table 1 - Contributions to understeer gradient, light truck [5.4]

| Factor | Front: CC_f | Rear: CC_r | $CC_f - CC_r$ |
|----------------------------------------|---------------|--------------|---------------|
| Tyre cornering stiffness $C_{F\alpha}$ | 5.9 | 7.5 | -1.6 |
| Roll steer | 1.0 | -1.5 | 2.5 |
| Camber | 0.2 | 0.0 | 0.2 |
| Lateral force compliance | 1.0 | 0.0 | 1.0 |
| Aligning torque | 0.8 | -1.4 | 2.2 |
| Steering compliance | 1.0 | 0.0 | 1.0 |
| Cornering compliance | 9.9 | 4.6 | |
| Understeer Gradient | | | 5.3 |

These terms include contributions from the tyre characteristics (cornering stiffness) as well as from other effects like aligning torque, compliance, camber effects, etc. In [Bickerstaff: 5.4], a breakdown of such contributions is given for a light truck, see [table 1](#)

It is clear from these tables that tyre characteristics have a strong impact on the cornering compliance, but these front and rear contributions tend to balance one another in the steering gradient. For a light truck, this even results in a negative gradient which indicates a potentially unstable situation. Due to all the other contribution, the final gradient is large and positive, even much larger than for the passenger car. This has to do with the fact that large differences in payload (as expected for a light truck) should keep this value positive. For both vehicles, roll steer and aligning torque appear to be the dominant factors in the total understeer gradient.

We shall now give some possible definitions of understeer behaviour:

Definition 1.

A vehicle is understeered if the steering angle has to be increased for increasing vehicle forward speed to negotiate the same curve. A vehicle is oversteered if the opposite is true, i.e. the steering angle has to be decreased for increasing vehicle forward speed to negotiate the same curve. We call a vehicle neutrally steered if no adjustment of δ is required.

Definition 2.

A vehicle is understeered if the front axle slip angle exceeds the rear axle slip angle under steady state conditions: $\alpha_1 > \alpha_2$.

Definition 3.

A vehicle is understeered if the understeer gradient $\eta > 0$, i.e. the normalized axle cornering stiffness front is exceeded by the normalized axle cornering stiffness aft. Note that:

$$\eta \cdot C_1 < 0 \quad (\text{Eq 21})$$

in case that η is not equal to 0, and where C_1 was defined in (Eq 9).

We conclude that, for linear tyre characteristics, all three definitions are identical. The understeer property is directly related to the steering wheel gradient, related to the steady state circular behaviour. That means that, under the restriction of linear tyre behaviour, the following alternative definition of understeer may be introduced:

Definition 4.

A vehicle is understeered if the steering wheel gradient $\partial\delta/\partial a_y > 0$.

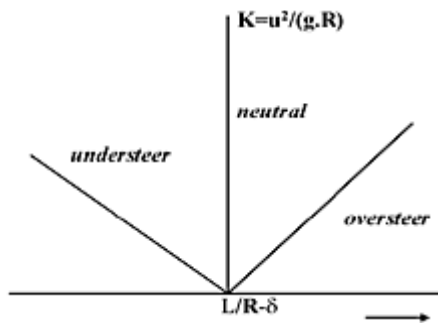


Figure 3 - Handling curve

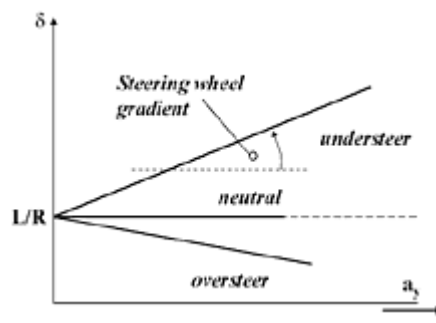


Figure 4 - Steering wheel angle characteristics

Two type of plots are shown in figure 3 and figure 4, with the one in figure 3 referred to as the handling curve and the one in figure 4 referred to as the steering wheel characteristics plot and usually drawn from the results of steady state circular test. Clearly one plot is found by rotating the other over 90°.

The under/oversteer factor K_δ is defined as the steering wheel gradient, taken at the steering wheel and expressed in degrees instead of radians. That means that the steering wheel gradient taken at the front axle should be multiplied by the steering ratio i_s (ratio of steering wheel angle at the steering wheel, and δ at the front wheels). From (Eq 16) one finds:

$$K_\delta = -\frac{m \cdot C_{1i}}{l \cdot C_{Fz1} \cdot C_{Fz2}} \cdot \frac{180}{\pi} = \frac{\eta \cdot i_s}{g} \cdot \frac{180}{\pi} ; [^\circ \text{ s}^2 \text{ m}^{-1}] \quad (\text{Eq 22})$$

Now let us examine this understeer behaviour more closer. We have defined it, but not explained the meaning of it. We'll continue to assume linear tyre

behaviour and solve (Eq 2) with all derivatives taking equal to zero.

One finds:

$$\left(\frac{r}{\delta}\right) = \frac{u.l.C_{Fz1}.C_{Fz2}}{l^2.C_{Fz1}.C_{Fz2} - m.u^2.C_1}$$

$$\left(\frac{\beta}{\delta}\right) = \frac{b.l.C_{Fz1}.C_{Fz2} - a.C_{Fz1}.m.u^2}{l^2.C_{Fz1}.C_{Fz2} - m.u^2.C_1} \quad (\text{Eq 23})$$

with the side slip angle β derived from the lateral velocity.

Define the stability factor K_s :

$$K_s = -\frac{m.C_1}{l^2.C_{Fz1}.C_{Fz2}} = \frac{1}{g.l}.\eta \quad (\text{Eq 24})$$

The steady state gains (Eq 23) can now be written as

$$\left(\frac{r}{\delta}\right) = \frac{u}{l.(1+K_s.u^2)}$$

$$\left(\frac{\beta}{\delta}\right) = \frac{b - B.u^2}{l.(1+K_s.u^2)} \quad ; \text{ where } B = \frac{a.m}{l.C_{Fz2}} \quad (\text{Eq 25})$$

From these expressions, it is easily concluded that yaw rate and side slip angle become unbounded for certain critical vehicle speed u_{cr} for an oversteered vehicle ($\eta < 0$, and therefore $K_s < 0$).

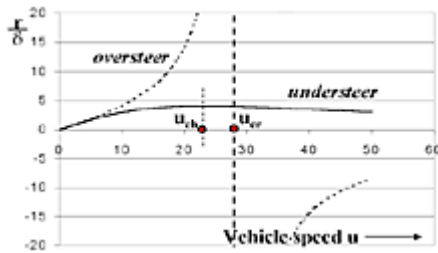


Figure 5 - Steady state yaw-rate gain

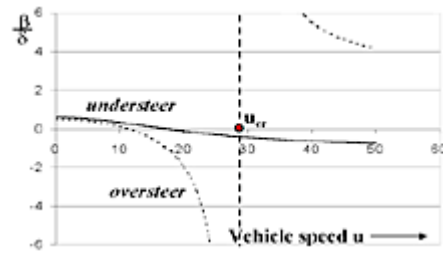


Figure 6 - Steady state sideslip angle gain

The expression for the critical speed is found from:

$$u_{cr}^2 = -\frac{1}{K_s} = -\frac{g.l}{\eta} = \frac{l^2.C_{Fz1}.C_{Fz2}}{m.C_1} \quad (\text{Eq 26})$$

To get an idea about the order of magnitude, we'll consider two vehicles:

Table 2

| | l [m] | a [m] | b [m] | $C_{F\alpha 1}$ [N/rad] | $C_{F\alpha 2}$ [N/rad] | m [kg] |
|------------|-------|-------|-------|----------------------------|----------------------------|-----------|
| Understeer | 2.8 | 1.1 | 1.7 | 7.E4 | 9.E4 | 1250 |
| Oversteer | 2.8 | 1.4 | 1.4 | 9.E4 | 6.E4 | 1250 |

For the oversteered vehicle, one obtains $u_{cr} = 28$ m/s

The gains (Eq 25) are shown graphically in [figure 5](#) and [figure 6](#), for these two vehicles.

One observes an asymptote at $u = u_{cr}$. One also observes the signchange in the sideslip angle β . For small vehicle speed, the steer angle is close to the Ackermann angle meaning that the total speed vector points inward with respect to the vehicle symmetry plane, corresponding with positive lateral speed v and thus $\beta > 0$. With increasing vehicle forward speed u , the total speed vector moves outward and the lateral speed will change sign.

We'll examine [figure 5](#) in more detail. For an oversteered vehicle, the relationship between yaw-rate and vehicle speed (for $u < u_{cr}$) is described by a concave curve. For an understeered vehicle, this relationship yields a convex curve, which has a maximum value u_{ch} , denoted as the characteristic speed u_{ch} . Differentiation of (Eq 25) leads to:

$$u_{ch}^2 = \frac{1}{K_s} = \frac{g \cdot l}{\eta} = - \frac{l^2 \cdot C_{F\alpha 1} \cdot C_{F\alpha 2}}{m \cdot C_1} \quad (\text{Eq 27})$$

For the vehicle as described by the above table, one finds $u_{ch} = 22.8$ m/s. Beyond this speed, the yaw-rate gain is reduced.

So far, we have examined vehicle behaviour under the assumption of linear tyre behaviour. We will now examine whether the foregoing results can be extended to full nonlinear tyre behaviour, meaning here nonlinearity with respect to slip-angle. We start with (Eq 12) and (Eq 13) again.

The first step is to invert (Eq 12) where we denote:

$$g_i(a_y) = \text{inv}[f_{y_i}(\alpha_i)](a_y) \quad ; i=1,2 \quad (\text{Eq 28})$$

The functions g_i are now multivalued functions in the lateral acceleration a_y (in g's, i.e. $K/(mg)$), where both single-valued branches may be treated separately.

It follows that:

$$\alpha_1 - \alpha_2 = \delta - \frac{l}{R} = g_1(a_y) - g_2(a_y) \equiv h(a_y) \quad (\text{Eq 29})$$

This relationship is the nonlinear extension of (5.16), where the linear term $\eta \cdot a_y$ is replaced by $h(a_y)$. It follows that the handling curve, the linear

simplification of which is shown in [figure 3](#), can be obtained by vertical subtraction of g_1 and g_2 in the $a_y - \delta$ plane, i.e. by horizontal subtraction of the original normalized axle characteristic curves in the $\delta - a_y$ plane. Since the functions g_i are multivalued, there exist different ways to carry out this subtraction, i.e. different branches of the two functions g_1 and g_2 can be combined. For the time being, only the branches connected to the origin (vanishing slip angles) will be considered here. In [figure 7](#), this refers to the maximum of f_2 .

The approach is schematically shown in [figure 7](#). In the upper part of this figure, the normalized axle characteristics are subtracted horizontally, yielding the counterpart of [figure 3](#). for nonlinear tyres. And again, this resulting plot can be rotated 90° to get the steering wheel angle characteristics in case of the full nonlinear axle characteristics. This shows clearly that the vehicle steering characteristics depend directly on the axle (and thus the tyre) characteristics.

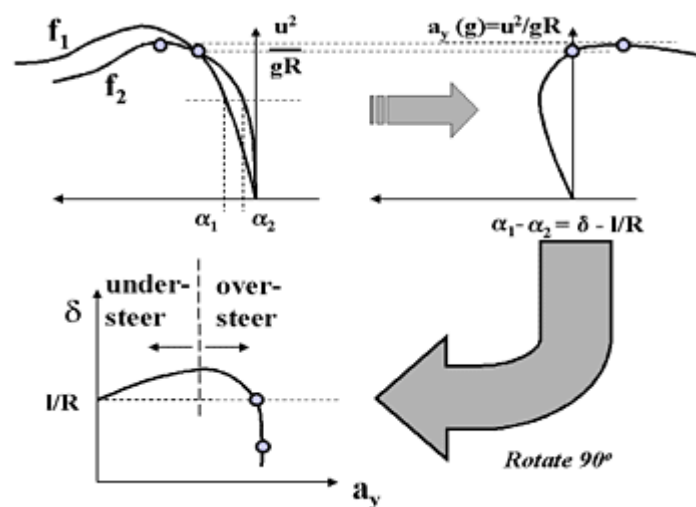


Figure 7 - Handling curve and steering characteristics, nonlinear tyre behaviour

As long as the steering angle δ , to negotiate the same curve (constant radius R), is increasing with growing lateral acceleration, we call the vehicle understeered. That means that definition 1 still holds. One observes in [figure 7](#) (as an example) two regions, one for understeer and one for oversteer. This partition is strongly dependent on the axle characteristics, and qualitatively different plots can be obtained for other tyre behaviour as we shall see later.

Just beyond the point of neutral steer (horizontal slope in $\delta = \delta(a_y)$), we still have $\delta > l/R$, and hence $\alpha_1 > \alpha_2$, cf. (Eq 15). That implies that definition 2 does not hold in the nonlinear case.

The understeer region corresponds to the situation where:

$$\frac{\partial f_{y1}(\alpha_1)}{\partial \alpha_1} < \frac{\partial f_{y2}(\alpha_2)}{\partial \alpha_2} \quad (\text{Eq 30})$$

showing that definition 3 still holds if η is replaced by

$$\eta_{\text{nonlinear}} = \frac{1}{\frac{\partial f_{y1}(\alpha_1)}{\partial \alpha_1}} - \frac{1}{\frac{\partial f_{y2}(\alpha_2)}{\partial \alpha_2}} \quad (\text{Eq 31})$$

A similar generalisation of *definition 4* can be derived as follows. Take the derivative of (Eq 12) with respect to a_y (now taken in m/s^2 , i.e. equal to u^2/R). This leads to:

$$\frac{1}{g} = \frac{\partial f_{y1}(\alpha_1)}{\partial \alpha_1} \cdot \frac{\partial \alpha_1}{\partial a_y} = \frac{\partial f_{y2}(\alpha_2)}{\partial \alpha_2} \cdot \frac{\partial \alpha_2}{\partial a_y}$$

and using the derivative of (Eq 15) with respect the a_y , one arrives at:

$$\frac{\partial \delta}{\partial a_y} = \frac{1}{g} \cdot \left(\frac{1}{f'_{y1}(\alpha_1)} - \frac{1}{f'_{y2}(\alpha_2)} \right) \quad (\text{Eq 32})$$

being the generalized version of the steering wheel gradient, indicated in [figure 4](#).

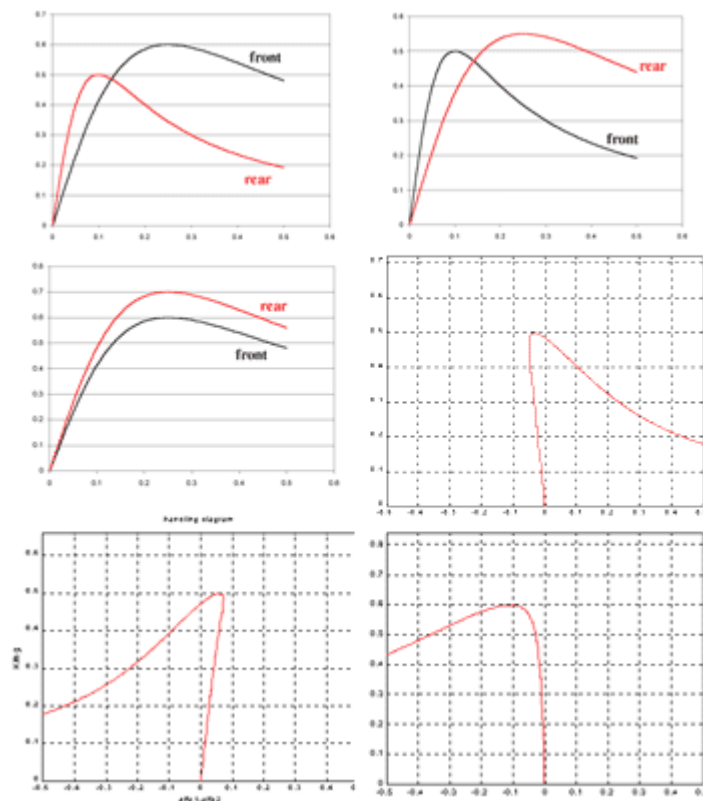


Figure 8 - Some examples of handling curves. Top: normalized axle characteristics. Bottom: corresponding handling curves

In figure 8, three different combinations of normalized axle characteristics are shown, from left to right:

- Understeer for small a_y , and oversteer for large a_y

- Oversteer for small a_y , understeer for large a_y
- Understeer for all a_y

The corresponding handling curves are shown below the axle characteristics. The first one is similar to the curve in [figure 7](#). One observes that the handling curve 'flips' horizontally if the understeer behaviour is changed into an oversteer behaviour.

The single track vehicle model, dynamic analysis and stability

In this section, we'll discuss the solutions of the equations of motion (Eq 2, previous chapter). In the preceding section, the steady state solutions of (Eq 2, previous chapter) have been treated, where we observed the relevance of the so-called understeer/oversteer properties with respect to the vehicle steady state behaviour.

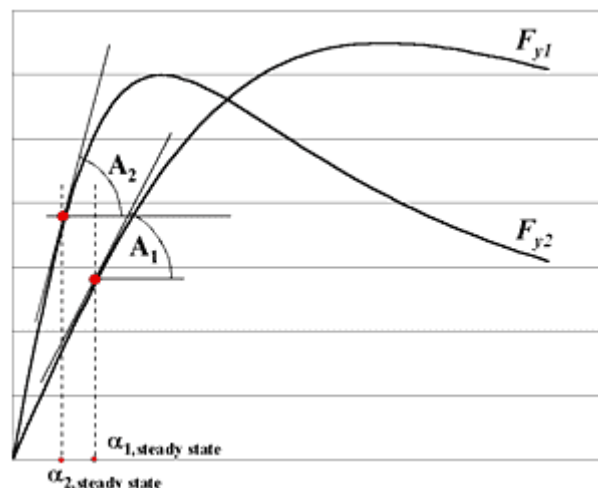


Figure 1 - Axle characteristics and steady state solutions

Let us now discuss stability of these steady state solutions, where we replace J_z by m.a.b. Hence, we'll linearize around the steady state solutions and discuss the nontrivial solutions of the resulting set of homogeneous equations. Let the slope of the axle characteristics front and rear be denoted by A_1 and A_2 , respectively (see [figure 1](#)). Note that, in general, these slopes are not the same as the cornering stiffness (which are taken at zero slip angle). Linearization leads to equations in $\Delta r = r - r_{\text{steady state}}$ and $\Delta v = v - v_{\text{steady state}}$. Substitution of (Laplace Transformation):

$$\Delta r = B_r e^{st} \quad ; \quad \Delta v = B_v e^{st}$$

leads to the system:

$$\begin{pmatrix} m.s + \frac{A_1 + A_2}{u} & mu + \frac{a.A_1 - b.A_2}{u} \\ \frac{a.A_1 - b.A_2}{u} & m.a.b.s + \frac{a^2.A_1 + b^2.A_2}{u} \end{pmatrix} \begin{pmatrix} B_v \\ B_r \end{pmatrix} = \begin{pmatrix} 0 \\ 0 \end{pmatrix} \quad (\text{Eq 1})$$

Nontrivial solutions exist if $x = u.m.s$ satisfies the characteristic equation:

$$a.b.x^2 + x.(a.A_1 + b.A_2).l - mu^2.\theta + l^2.A_1.A_2 = 0 \quad (\text{Eq 2})$$

where:

$$\theta = a.A_1 - b.A_2 \quad (\text{Eq 4})$$

From comparison with (Eq 31, previous chapter) it is easily seen that

$$\theta = -\eta_{\text{nonlinear}}.A_1.A_2 \quad (\text{Eq 5})$$

meaning that understeer behaviour corresponds to $\theta < 0$.

Bounded solutions (to guarantee stability) imply $\text{Re } s < 0$. For this quadratic equation (Eq 2), it is easy to see that this condition is fulfilled if:

$$a.A_1 + b.A_2 > 0 \quad \text{and} \quad -mu^2.\theta + l^2.A_1.A_2 > 0 \quad (\text{Eq 6})$$

If $\theta < 0$ (understeer), then the second condition is automatically fulfilled for slopes $A_1, A_2 > 0$. In this case, the first condition is fulfilled as well, and the vehicle will be stable for all speeds. However, if $\theta > 0$, the second condition is only fulfilled if the vehicle speed u is bounded by the critical speed u_{cr} :

$$u < u_{cr} = \left[\frac{l^2}{m} \cdot \frac{A_1.A_2}{a.A_1 - b.A_2} \right] = - \frac{l^2}{m.\eta_{\text{nonlinear}}} \quad (\text{Eq 7})$$

being the nonlinear generalisation of (Eq 26, previous chapter).

If $A_1.A_2 < 0$ and $\theta < 0$ then necessarily $A_1 < 0$ and $A_2 > 0$ meaning severe drifting of the vehicle at the front axle. The second condition of (Eq 6) now implies stability only if the vehicle speed u is bounded below, i.e. if one drives fast enough:

$$\text{if } A_1 < 0, A_2 > 0, a.A_1 + b.A_2 > 0 \text{ then} \\ u > u_{cr} = \left[\frac{l^2}{m} \cdot \frac{-A_1.A_2}{-\theta} \right] \text{ implies stable behaviour} \quad (\text{Eq 8})$$

Hence, even with the front part of the vehicle showing severe understeer behaviour, the vehicle can be kept stable as long as the speed u is sufficiently high. The first condition of (Eq 6) corresponds to

$$\frac{df_{y1}(\alpha_1)}{d\alpha_1} + \frac{df_{y2}(\alpha_2)}{d\alpha_2} > 0$$

while θ can be written as:

$$\theta = \frac{mgab}{l} \left(\frac{df_{y1}(\alpha_1)}{d\alpha_1} - \frac{df_{y2}(\alpha_2)}{d\alpha_2} \right) \quad (\text{Eq 9})$$

The different stability areas can therefore be indicated in the f_{y1} - f_{y2} plane, as shown in [figure 2](#). The curved boundaries of the two conditional areas ($u < u_{cr}$ and $u > u_{cr}$, respectively) are hyperbolic curves, which follows easily from the second condition of (Eq 6). Changing the speed u means that the asymptotes to these curves will move, changing the stability area outside the understeer range. Indeed, with increasing u , the stability area in the first quadrant will be reduced whereas the stability area in the fourth quadrant is extended. With decreasing u , the opposite is true.

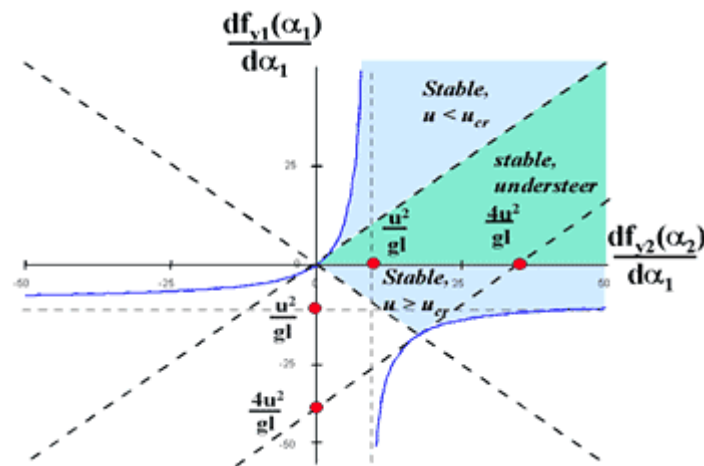


Figure 2 - Stability areas

The dynamic behaviour of solutions of (Eq 2, previous chapter) may be studied in the phase plane, with state vector (α_1, α_2) , cf. (Eq 7, previous chapter). Clearly, solution lines (trajectories) will either move to the singular points corresponding to steady state solutions of (Eq 2, previous chapter) or vanish to infinity. Some examples are shown in [figure 3](#), [figure 4](#) and [figure 5](#) below, corresponding to the following cases (see also figure 8):

- understeered vehicle
- stable oversteered vehicle (below critical speed)
- unstable oversteered vehicle (beyond critical speed: $v < v_{crit}$)

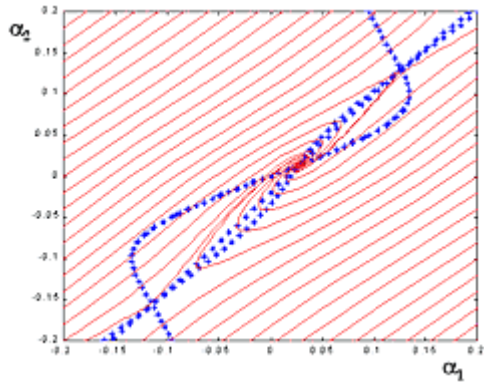


Figure 3 - Phase plane representation; Understeered vehicle

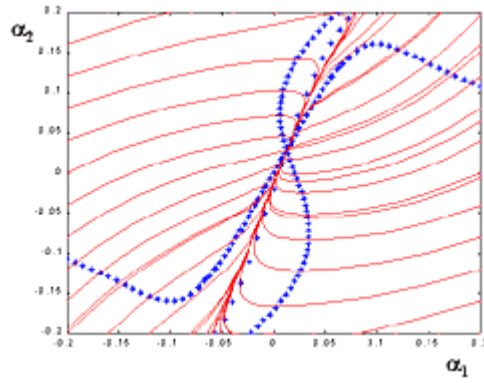


Figure 4 - Phase plane representation; Oversteered vehicle, $v < v_{crit}$

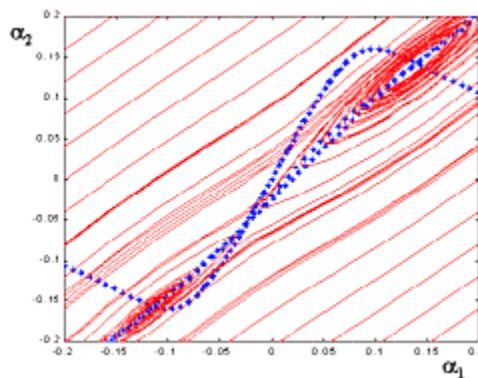


Figure 5 - Phase plane representation; Oversteered vehicle, $v > v_{crit}$

Axle characteristics have been chosen such that three steady state solutions may exist. The same figures also show (in blue) the isoclines corresponding to a fixed slope of the solution curves (horizontal, vertical, under 45°). Intersections of these isoclines coincide with the singular points.

In case of an understeered vehicle, a stable focus arises in the middle with two unstable saddle points for the other two steady state conditions. This means that initial conditions should not be too far off from this stable point in order to guarantee the solution to approach this point as t approaches infinity. In other words, the attraction area of this point is bounded with boundary built up from the manifolds of both saddle points. Consequently, the non-stable singular points determine the attraction area of the stable steady state solution.

In case of an oversteered vehicle for sufficiently large speed, the intermediate steady state solution has turned into an unstable point (as expected) being a saddle point in between two stable focus points. This unstable point is known to turn into a stable one with decreasing vehicle speed, as observed in [figure 3](#). This time, a stable two-tangent node is obtained as singular point. So far, we have discussed singular (steady state) points and the type of stability with distinction in divergent instability (saddle points), oscillatory (in-) stability (focus point), convergent stability (two-tangent node), etc.

We shall treat both aspects more in detail. For further interpretation of stability and the occurrence of several steady state solutions in terms of forward speed u and steering angle δ , the so-called handling diagram offers many advantages.

We now follow the same approach as indicated in the preceding section cf. figure 7

in chapter "The single track vehicle model", this time with all branches included. The result of this exercise is shown in [figure 6](#) for a certain combination of axle characteristics, indicating clearly the strong impact of axle (i.e. tyre) characteristics on vehicle steering performance.

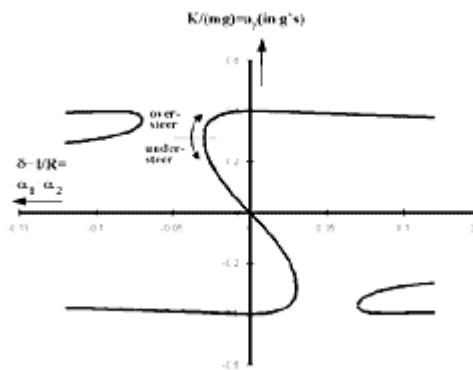


Figure 6 - Handling diagram, first step

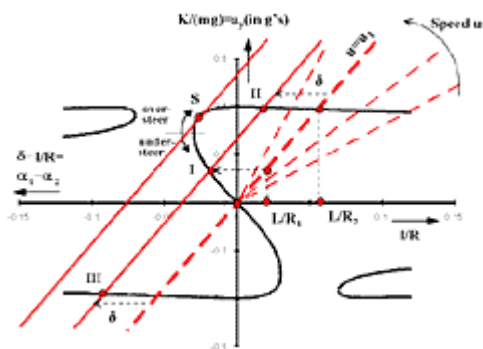


Figure 7 - Handling diagram

This result (handling curve) will be merged with another diagram having the ordinate $K/(mg)$ yielding the so-called handling diagram. From (Eq 12, previous chapter), one observes that the side force K depends linearly on the path curvature $(a+b)/R$ is identically equal to l/R , i.e. corresponding to a family of straight lines with slope proportionally to the square of the vehicle speed. According to (Eq 29, previous chapter), these curves and the diagram in [figure 6](#) combine to produce the steer angle as the horizontal distance between the handling curve ([figure 6](#)) and these straight lines, see [figure 7](#).

For a better understanding, the application of the handling diagram as depicted in [figure 7](#), is discussed step by step. Assume a path-radius R_1 (i.e. path curvature l/R_1) and a vehicle forward speed u_1 . That means that the point $(l/R, K/(mg))$ is lying on the straight line with slope $(u_1^2/(g.l))$. Because of (Eq 29, previous chapter), applying a steering angle δ means that this line is shifted to the left over a horizontal distance δ .

As a result, steady state solution I is found, lying in the understeer region. For very small speed u , the corresponding straight line is almost coinciding with the horizontal axis, and consequently, the necessary steering angle to reach the origin equals l/R , the Ackermann angle. For speed u_1 and steering angle δ , three steady state solutions arise, denoted as I, II and III as long as δ is not too large. For a certain value of δ , $\delta = \delta_s$ the point S is reached (see [figure 7](#)) and beyond this value, the number of three steady state solutions drops down to 1 (which must be unstable).

Now assume the steering angle δ to be chosen below δ_s but close to it, and consider the resulting steady state solution I. Slightly increasing the lateral acceleration a_y implies increase of the steering angle in order to reach a new steady state solution. That means that I is stable as long as it is situated below S. In the same way one may conclude that, for the steady state solution II lying above S, increase of a_y would involve reduction of steering angle δ yielding a self-reinforcing effect (further increase of a_y), leading to yaw-instability.

This kind of instability can only occur if the vehicle behaves oversteered, i.e. when the slope of the handling curve is positive. Decreasing of the speed u leads to increase of the lateral acceleration where the steering angle is maximal. This maximum steering angle increases as well with decreasing u . Consequently,

stability is improved.

Instability occurs in points II and III where the slopes are negative but where one of the axle characteristics (rear axle) shows a downward slope at the α concerned.

Analysis of the coefficients of the characteristic equation for the disturbed motion around an equilibrium point reveals the question of stability, as indicated in [Figure 2](#). Also, the nature of stability (monotonous, oscillatory) follows from these coefficients. This is reflected in the type of singular points (node, saddle, focus) as discussed earlier. This analysis has been carried out with the results added to [Figure 2](#). This results in the diagram of [Figure 8](#).

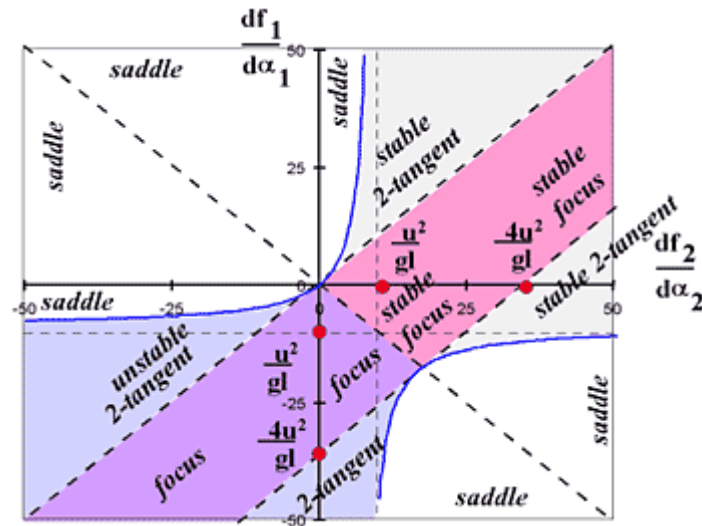


Figure 8 - Stability areas and types of singular

This diagram shows areas with similar type of singular points, depending on the value of cornering stiffness for the normalised axle characteristics. The boundaries of these areas depend on vehicle velocity u . Clearly, the part of the diagram for large negative values of these normalised cornering stiffnesses are only relevant for theoretical reasons, i.e. to illustrate the typical pattern of these areas. However, observe that the cases in the lower half of the diagram may occur for excessive vehicle behaviour for small u .

The stable and unstable regions excluding the saddle points are distinguished by a slightly lighter colour for the stable regions. [Figure 8](#) reveals that stable steady state solutions are either two-tangent nodes or a stable focus.

A stable oversteered vehicle with positive axle cornering stiffnesses will correspond to a two-tangent node, i.e. with disturbances (such as in case of a J-turn) approaching it in a monotonous way without oscillations. As long as u^2 is bounded by $g.l.[f_{y2,\alpha}(\alpha_2) - f_{y1,\alpha}(\alpha_1)]$ in the understeer region, the steady state solution corresponds to a stable focus. Beyond this speed, this focus turns into a stable two-tangent node. In the situation of excessive understeer ($f_{y1,\alpha}(\alpha_1) < 0$), a same distinction can be made.

These regions are more or less flipped to the unstable area leading to unstable two-tangent nodes and unstable focus. In all the other cases, the singular point is a saddle point.

In [6.1], several results regarding stability of single trucks were discussed by Pacejka, with results confirmed by Winkler in [5.8].

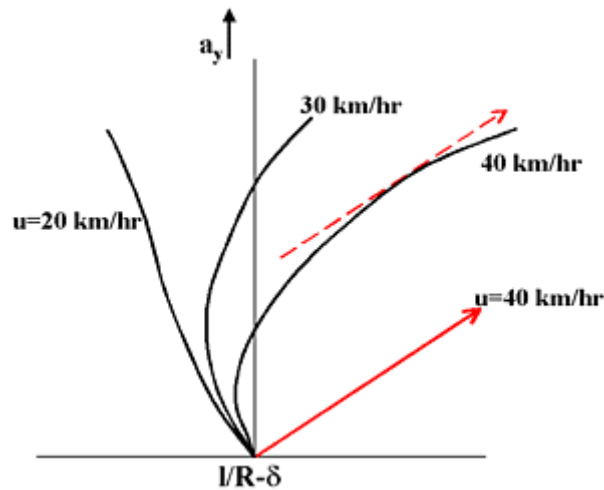


Figure 9 - Handling diagrams, depending on speed u for complex axle configurations

As discussed above (referring to the work of Winkler and Pacejka), it was mentioned that tandem axles and dual tyres make the relationship between steering angle and lateral acceleration depending on both a_y and path curvature. Alternatively, one may write this relationship in terms of a_y and vehicle velocity u . To understand this, one should be aware of the fact that tandem axles and dual tyres produce a moment that counteract the rotation of the truck, i.e. lead to more understeer or less oversteer. To formulate this in terms of the steering angle, an increased steering angle is required to compensate these effects. Consequently, the handling diagram is shifted more to the left. Since this effect is most strong at low vehicle speed, this shift is speed dependent and most pronounced for small speed. These shifts are indicated in [figure 9](#).

Yaw stability of articulated trucks

We now discuss an articulated vehicle, as schematically shown in [figure 1](#) below.

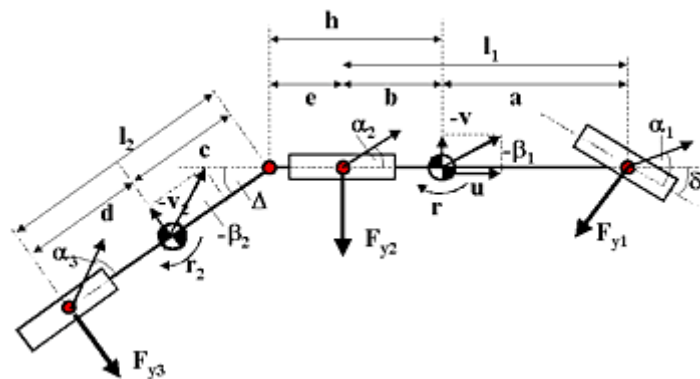


Figure 1 - Articulated vehicle model

Roll-motion will be neglected, steer and slip angles will be assumed small, driving forces and braking forces are small compared to lateral forces or are neglected. Consequently, a similar approach will be followed as for the single vehicle but this time with the articulation angle Δ as an additional state. All wheels for one axle are taken as one system with overall characteristics and response. That means that tyre characteristics are again replaced by axle characteristics. Forward speed u is taken constant and pneumatic trails (i.e. aligning torques) are neglected.

Masses are denoted as m_1 for the first articulation (tractor, car) and m_2 for the second articulation (trailer, caravan,...). The polar moments of inertia are denoted as J_1 and J_2 , respectively.

The equations of motion can be derived from the statements that equilibrium must hold in lateral and yaw direction. The lateral tyre forces must balance the lateral vehicle accelerations at both vehicle-parts. Moreover, the yaw moment acting on each of the articulations must be balanced by the moment due to the tyre forces plus the moment resulting from the internal reaction force at the articulation point. This leads to the equations (see [figure 1](#) for notation):

$$\begin{aligned} (m_1 + m_2)(\dot{v} + ur) - m_2[(h+c)\dot{\Delta} - c\dot{\Delta}] &= F_{y1} + F_{y2} + F_{y3} \\ [J_1 + m_2 h(h+c)]\dot{r} - m_2 h[\dot{v} + ur + c\dot{\Delta}] &= aF_{y1} - bF_{y2} - hF_{y3} \\ (J_2 + m_2 c^2)(\dot{r} - \dot{\Delta}) + m_2 c[\dot{v} + ur - h\dot{\Delta}] &= (c+d)F_{y3} \end{aligned} \quad (\text{Eq 1})$$

in terms of lateral speed v and yaw rate r , both of the first vehicle (tractor), and the articulation angle Δ . The slip angles at the three axles are derived similar to (Eq 6, in "The single track vehicle model"), leading to:

$$\begin{aligned} \alpha_1 &= \delta - \frac{v + a.r}{u} \\ \alpha_2 &= -\frac{v - b.r}{u} \\ \alpha_3 &= -\Delta - \frac{v - (h+l_2).r + l_2.\dot{\Delta}}{u} \end{aligned} \quad (\text{Eq 2})$$

We'll discuss first the steady state situation, where the above equations reduce to:

$$\begin{aligned} (m_1 + m_2)ur &= F_{y1} + F_{y2} + F_{y3} \\ -m_2 h.ur &= a.F_{y1} - b.F_{y2} - h.F_{y3} \\ m_2 c.ur &= (c+d).F_{y3} \end{aligned} \quad (\text{Eq 3})$$

and

$$\alpha_3 = -\Delta - \frac{v - (h + l_2) \cdot r}{u} \quad (\text{Eq 4})$$

Observe that

$$\alpha_2 - \alpha_3 = \Delta - \frac{(e + l_2)}{R} \quad (\text{Eq 5})$$

Finding expressions for the lateral axle forces, one finds similar to (Eq 13, in "The single track vehicle model") for the normalised axle characteristics that

$$f_{y1} = f_{y2} = f_{y3} = \frac{K}{m \cdot g} \quad (\text{Eq 6})$$

which can again be inverted leading to multi-valued functions of α_i in terms of $K/(mg)$. That means that a handling diagram can be established giving steady state solutions in terms of $\alpha_1 - \alpha_2$ and lateral acceleration a_y for given steering angle δ just as this was established earlier. At the right-hand side of the diagram, one draws a_y versus l_1/R with path radius of curvature R according to:

$$\frac{K}{mg} = \left(\frac{u^2}{g \cdot l_1} \right) \cdot \frac{l_1}{R} \quad (\text{Eq 7})$$

In the same figure, a handling diagram can be established giving steady state solutions in terms of $\alpha_2 - \alpha_3$ and lateral acceleration a_y for given articulation angle Δ . At the right-hand side of the diagram, one now draws a_y versus $(l_2 + e)/R$ (as suggested by (12)):

$$\frac{K}{mg} = \left(\frac{u^2}{g \cdot (l_2 + e)} \right) \cdot \frac{l_2 + e}{R} \quad (\text{Eq 8})$$

For a typical case of a tractor-trailer with normalised tyre characteristics as shown in [figure 2](#), this analysis has been carried out, with the result depicted in [figure 3](#).

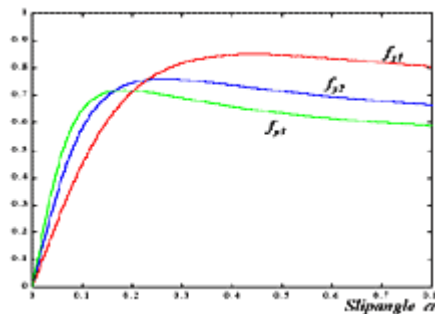


Figure 2 - Normalized axle characteristics

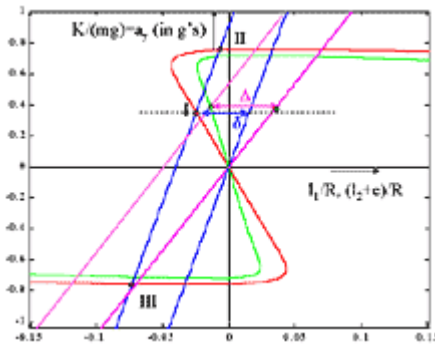


Figure 3 - Handling diagram articulated vehicle

The handling curve related to first and second axle is shown in red. The handling curve related to the second and the third axle is shown in green.

The tyre characteristics were chosen to obtain an illustrative handling diagram. Selected parameters are listed in table 1, below.

Table 1 - Parameters, tractor-semitrailer

| a (m) | b (m) | c (m) | d (m) | e (m) |
|--------|--------|---------|---------|-------|
| 1.5 | 2.5 | 6.0 | 3.0 | -0.5 |
| m1(kg) | m2(kg) | d (rad) | u (m/s) | |
| 5000 | 20000 | 0.06 | 20 | |

Two straight lines are shown, blue and purple relating to (Eq 7) and (Eq 8), respectively. Shifting the first over a steering angle δ and intersecting with the handling curve for the axles 1 and 2, leads to three steady state solutions, one of which is stable in yaw (I). As discussed above, this solution determines the lateral acceleration at hand, and from this the articulation angle being the horizontal distance between the straight line according to (Eq 8) and the $\alpha_2 - \alpha_3$ curve.

Having determined the steady state solutions in this graphical way, one may consider their stability. The handling diagram can be used to interpret yaw stability and divergent yaw-instability. Oscillating phenomena require a full treatment of the linearised equations based on (Eq 1). In [figure 3](#), one may conclude just like for the single vehicle in the preceding section, that increasing the lateral acceleration starting from situation I implies that the steering angle δ must increase as well. At the same time, the articulation angle Δ will increase as well. That means that for both the tractor and the trailer, there is a compensating effect for the increased lateral acceleration and this effect was related to stability in the preceding sections.

We shall continue with cases where at either the tractor or the trailer, these conclusions cannot be drawn.

Replace normalized tyre characteristics such that the highest cornering stiffness is obtained at the second axle and the lowest cornering stiffness is obtained at the rear axle. These characteristics are shown in [figure 4](#). That means that for limited lateral acceleration, the tractor as a single vehicle, is understeered whereas the trailer with the second axle regarded as its leading and steering axle can be regarded as oversteered.

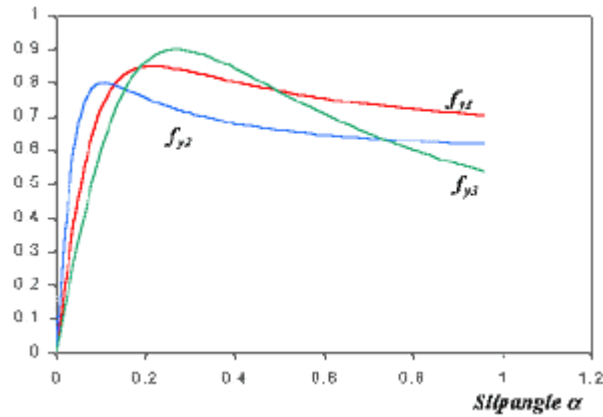


Figure 4 - Normalized axle characteristics, trailer oversteered

Two handling diagrams (enlarged) have been determined for input steering angle 0.05 rad. and different speeds:

$$u_1 = 18 \text{ m/s}$$

$$u_2 = 40 \text{ m/s.}$$

The handling diagrams are shown in [figure 5](#) and [figure 6](#).

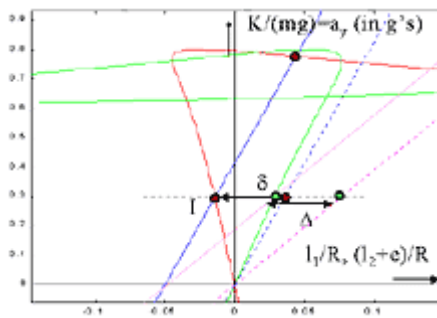


Figure 5 - Handling diagram, u = 18 m/s

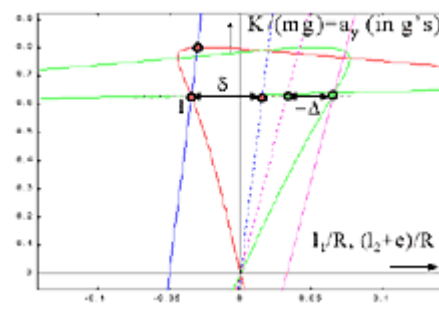


Figure 6 - Handling diagram, u=40 m/s

Again, take the steady state solution as starting point and consider steady state solutions for slightly larger lateral accelerations. That means that the steady state point will move up in the figures. In both [figure 5](#) and [figure 6](#) the steering angle δ will have to increase. However, considering the articulation angle Δ , this angle appears to change sign for vehicle speed changing from 18 m/s to 40 m/s. Starting from both steady state solutions, the angle Δ will increase with increasing a_y in figure 5 whereas it will decrease with increasing a_y in [figure 6](#). Consequently, in the last case, the trailer points inward and tries to follow a smaller path radius. Observe that steering angle and articulation angle have opposite signs. Apparently, the trailer 'runs the show' in determining the vehicle performance, where the understeered nature of the tractor keeps the vehicle stable. As soon as the critical lateral acceleration is reached (where the tractor becomes oversteered), divergent instability will occur, controlled by the trailer. This effect is referred to as trailer swing. Compare this situation with [figure 5](#) for low speed where steering angle and articulation angle both have the same sign, i.e. the tractor dominates the behaviour and the trailer follows the tractor response.

We shall come back to this type of instability later.

A more general way to visualize stability is to draw similar plots as figure 2 and 8 in previous chapter, i.e. $F_{y2,\alpha}$ versus $F_{y1,\alpha}$ for various values of $F_{y3,\alpha}$. We shall do that for two typical vehicle configurations:

- Tractor - semitrailer
- Truck with centre-axle trailer

The (artificially selected) data used for both configurations is shown in [table 2](#) and [table 3](#) below, with A_i denoting the values for axle cornering stiffness, setting the boundaries of the stability plot:

$$-A_i/4 < F_{y1,\alpha} < A_i$$

Table 2 - Parameters, tractor-semitrailer

| m1(kg) | m2(kg) | a(m) | l ₁ (m) | c(m) |
|--------------------|--------|--------------------|--------------------|--------------------|
| 5000 | 20000 | 1.5 | 4 | 6 |
| l ₂ (m) | e(m) | A ₁ (N) | A ₂ (N) | A ₃ (N) |
| 9 | -0.5 | 3.8E5 | 7.5E5 | 1.3E6 |

Table 3 - Parameters, truck & centre-axle trailer

| m1(kg) | m2(kg) | a(m) | l ₁ (m) | c(m) |
|--------------------|--------|--------------------|--------------------|--------------------|
| 8000 | 20000 | 4 | 8 | 4 |
| l ₂ (m) | e(m) | A ₁ (N) | A ₂ (N) | A ₃ (N) |
| 4 | 0.5 | 4E5 | 3E5 | 2E6 |

That means that we shall also consider negative slope of the axle characteristics under steady state conditions, ofcourse corresponding to the case of full sliding at that axle.

We'll discuss first the impact of moving the cog of the trailer backward up to $c = 8$ m. Assuming linear tyre behaviour with the cornering stiffness equal to A_i , root-locus plots for varying speed u have been established for $c = 6$ m (reference case) and $c = 8$ m (cog_{trailer} moved backward), see [figure 7](#). For small value of c , two types of eigenvalues turn out to exist, real ones and complex ones, corresponding to the motion of the tractors and the semitrailer, respectively. Moving the cog of the trailer backward will make the vehicle combination unstable in the trailer-mode, indicating trailer oscillations beyond a certain speed. The corresponding cornering stiffness plot for $u = 30$ m/s is shown in [figure 8](#), i.e. where the type of stability is indicated as a function of the actual slope of the lateral axle force, assuming full non-linear axle characteristics. This slope at the semitrailer axle is taken according to [table 2](#) (A_3). Note that the scales along both axes are not the same (cf. values of A_i in [table 2](#))

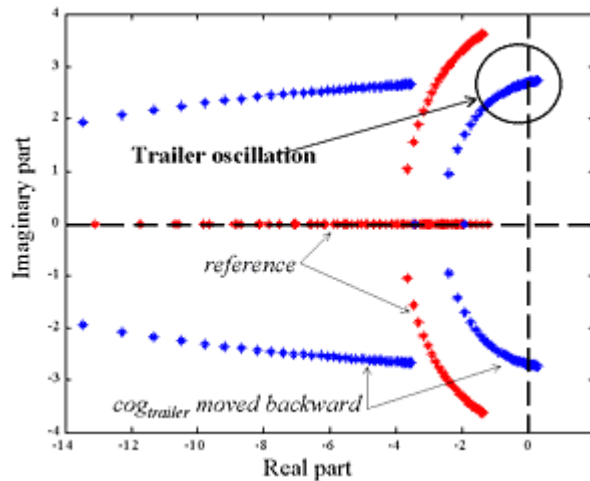


Figure 7 - Root-locus plot tractor-semitrailer

This plot clearly corresponds to [figure 8](#), with a stable area in the first quadrant, moving to divergent instability for decreasing slope of the lateral force at axle 2 (saddle point for a single vehicle), and moving to oscillatory instability for small negative slope at axle 1. The same plot for the cog of the trailer moved backward is shown in [figure 9](#).

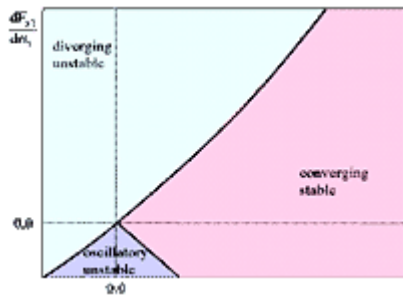


Figure 8 - Stability areas, reference case

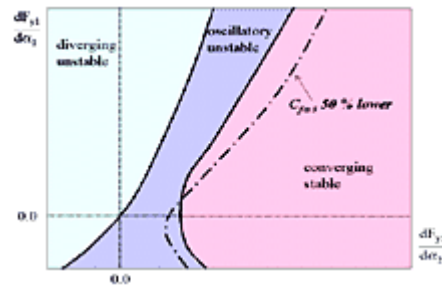


Figure 9 - Stability areas, cog_{trailer} moved backward

This plot shows a strong increase of the oscillatory instability area, corresponding to behaviour of the trailer and confirming the occurrence of trailer snaking phenomena around specific unstable steady state solutions. We have further decreased the slope of the trailer axle lateral force with 50 %. This resulted in a new boundary between the convergent stability area and the oscillatory instability area, indicated by a dash-dotted line. Consequently, the instability area will increase which is obvious from the reduced stiffness against yaw-oscillations of the trailer.

Next, we treat the truck with centre axle trailer, according to the data in [table 3](#). The axle characteristics have now been chosen such that unstable oversteer will occur for the tractor beyond a certain speed. That means that, in contrast to [figure 2](#), the normalized cornering stiffness at the tractor front axle exceeds the tractor rear axle normalized cornering stiffness. We'll discuss the impact of reducing the cornering stiffness of the trailer axle with 50 %. Again, first assuming linear tyre behaviour with the cornering stiffness equal to A_i as listed in [table 3](#), root-locus plots for varying speed u have been established for $A_3 = 2E6$ N (reference case) and $A_3 = 1E6$ N, see [figure 10](#). One observes divergent instability beyond a critical speed in the reference situations. Reducing the trailer axle cornering stiffness results in oscillatory instability at

much lower velocity compared to the initiation of divergent instability (oversteer). The corresponding stability areas for $u = 25$ m/s in terms of the cornering stiffnesses of the truck-axes are shown in [figure 11](#) and [figure 12](#), respectively.

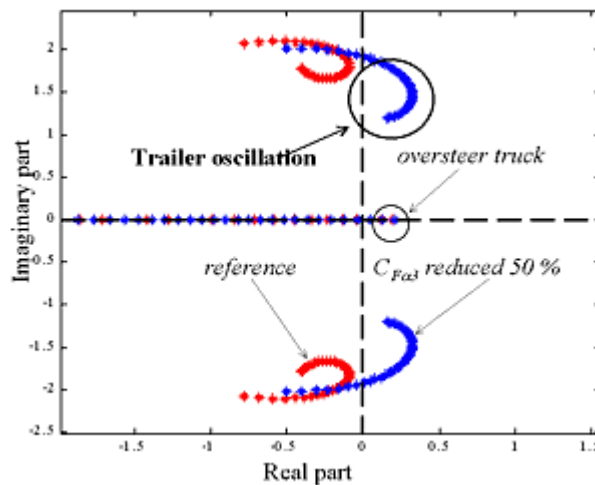


Figure 10 - Root-locus plot truck with centre-axle

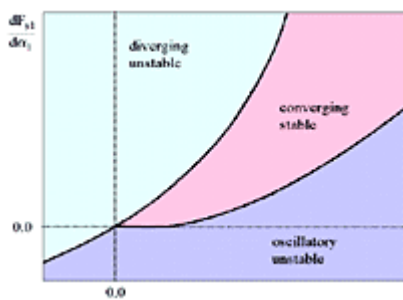


Figure 11 - Stability areas, centre-axle trailer, reference case

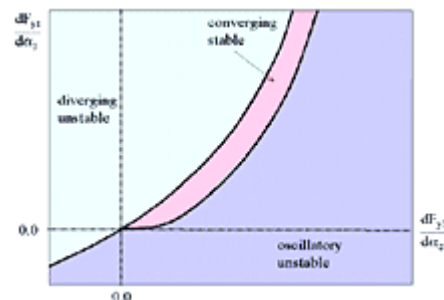


Figure 12 - Stability areas, centre-axle trailer, reduced cornering stiffness trailer axle

One observes in figure 11 three different stability areas, with the stable combinations surrounded by divergent instability and oscillatory instability. Reducing the cornering stiffness at the trailer axle results in a significant reduction of the stability area, i.e. leaving only a stable solution for very specific combinations of slopes of the truck axle characteristics.

In [7.1], results are discussed about the impact of design changes of a three-axle tractor, two-axle semitrailer combination on the handling diagram, for $u = 80$ km/h. It is shown that:

1. Only a strong increase of the tractor frame torsional stiffness does not result in a significant change in the handling diagram. This is attributed to the very low front suspension roll stiffness.
2. Consequently, increasing this roll stiffness appears to result in much more understeer compared to the reference situation.
3. The addition of frame stiffening yields a further increased tendency in understeer.

The following modifications with respect to the reference situation appeared to

degrade the tractor yaw stability (described by the handling diagram):

- a mix tyre combination with the lowest cornering stiffness mounted at the rear
- a stiffer tandem suspension, resulting in an increase of the contribution of the tractor to the vehicle roll during cornering
- a more rearward placement of the coupling plate between tractor and trailer
- a lower roll stiffness of the trailer suspension
- increased height of the payload

The above discussion revealed divergent instability for the tractor (jack-knifing due to oversteer) and oscillating instability induced by the trailer beyond a critical speed u_{cr} (trailer swing). It is argued in [6.1] that divergent instability may occur for the trailer in case the understeer gradient of the trailer (front wheel being the rear wheels of the tractor) as a ratio to the understeer gradient of the trailer is greater than the ratio of the respective wheel bases:

$$\frac{\eta_2}{\eta_1} > \frac{l_2}{l_1}$$

with subscripts 1 and 2 again related to first and second articulation. This discussion was based on the case $e = 0$. From the steady state equation (Eq 3), it can be found after some tedious calculations:

$$\frac{\Delta}{\delta} = \frac{g \cdot (l_2 + e) u^{-2} + \eta_2}{g \cdot l_1 u^{-2} + \eta_1} \quad (\text{Eq 9})$$

recalling that (see (Eq 16 in "The single track vehicle model"))

$$\eta_1 = \frac{F_{x1}}{C_{Fx1}} - \frac{F_{x2}}{C_{Fx2}} \quad ; \quad \eta_2 = \frac{F_{x2}}{C_{Fx2}} - \frac{F_{x3}}{C_{Fx3}} \quad (\text{Eq 10})$$

That means that for $\eta_i < 0$ there exist both an asymptote at:

$$u_{\sigma} = \left(\frac{g \cdot l_1}{-\eta_1} \right)^{\frac{1}{2}}$$

and a zero-value for Δ at

$$u_0 = \left(\frac{g \cdot (l_2 + e)}{-\eta_2} \right)^{\frac{1}{2}}$$

There are two typical situations, illustrated in [figure 13](#).

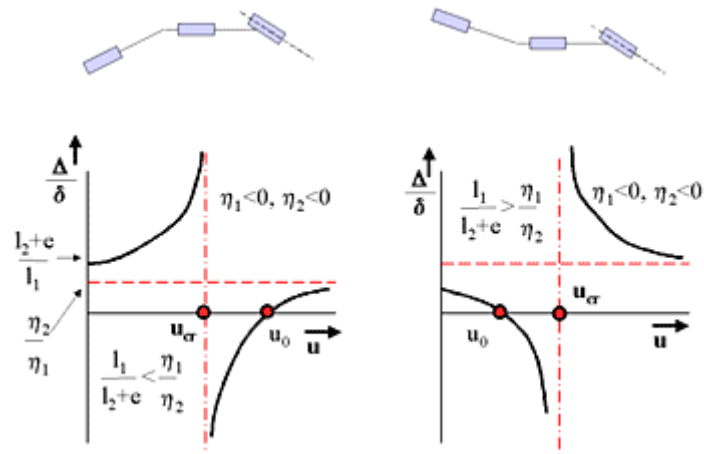


Figure 13 - Possible divergent instability of the trailer

If the tractor-instability controls the full vehicle, the left-hand side picture applies which is similar to figure 5 in chapter "The single track vehicle model". This case corresponds with jack-knifing with articulation angle and steering angle having the same sign with vehicle velocity close to the critical speed u_{cr} . However, if the trailer instability controls the full vehicle performance, the right-hand picture applies. The trailer and tractor move in the same direction with the trailer moving ahead of the tractor. As a result, the articulation angle and the steering angle have opposite sign. As the condition to decide about the situation at hand, the above inequality should be replaced by:

$$\frac{\eta_2}{\eta_1} > \frac{l_2 + e}{l_1} \quad (\text{Eq 11})$$

Modelling of tyres

We shall briefly discuss tyre modelling for an arbitrary tyre, i.e. not restricting to truck tyres.

Several kinds of mathematical models of the tyre have been developed, each for a specific purpose. At one end of the scale, one tries to describe tyre behaviour very accurately for reasons of tyre design (FEM tools, see [figure 1](#)) or to incorporate the correct tyre response in vehicle dynamics simulations (similarity approach, Magic Formula). At the other hand of the scale, one tries to describe the tyre in a physical way in order to understand the mechanisms that contribute to tyre performance. These models are not expected to give a very accurate correspondence with measurement but should predict the qualitative trends.

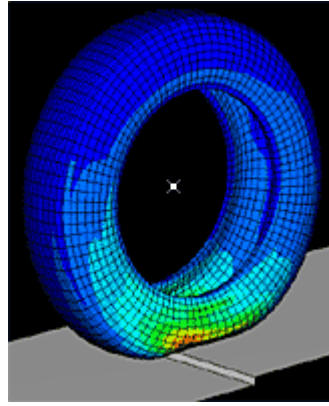


Figure 1 - FEM tyre model running over step

It is clear that both type of models should be considered. Quantitative models cannot be developed without a minimum notion of the tyre physical behaviour, obtained through simplified physical models. Qualitative models do not make sense without a spin-off that can be used in practical engineering applications. Each of these tyre models require extensive testing and experimental parameter assessment.

| | Qualitative understanding | Accurate, quantitative fit |
|-----------------------------------|-----------------------------------------------------------------------------------------------------------------------------------|---------------------------------------------------------------|
| Easy to handle, low effort | Physical models with treads modelled as brushes and/or with belt modelled as a string, possibly leading to a closed form solution | Empirical models, fitting of experimental data, Magic Formula |
| Difficult to handle, large effort | Flexible belt models, simplified FEM models | Finite Element Model |

Simplified physical models.

Physical models should account for:

- frictional properties in the tyre-road interface
- distribution of the normal contact force
- stiffness of the tread rubber
- stiffness of the carcass.

Neglecting carcass stiffness, and assuming Coulomb friction with dynamic and static friction taken equal, one arrives at the most simple so-called brush model. The response of the tyre to a shear force is accounted for by deformation of brush elements attached to a rigid carcass. These brush elements are little springs, deflected horizontally with certain spring stiffness under the action of local shear stresses in the contact area.

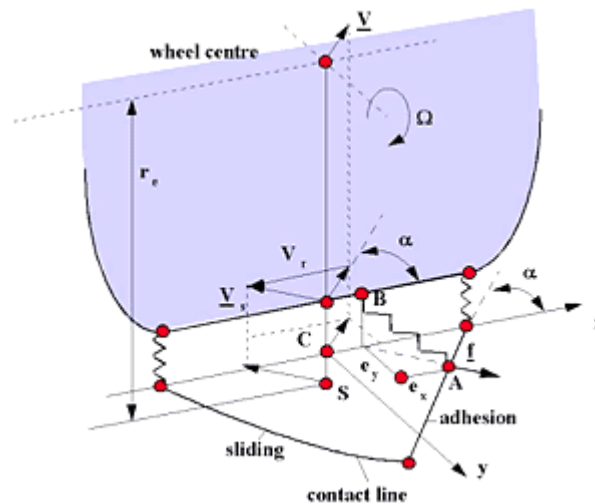


Figure 2 - Layout tyre brush model

Two regions are identified, an adhesion region where the contact line (connecting the tips of the brush elements) is straight, and a sliding region where the shear stress follows Coulombs law ($\tau = \mu \cdot \sigma_z$). In the above figure, the tyre is moving with speed V , built up from a rolling speed V_r and a slip speed V_s , with both a lateral and a longitudinal component. These components correspond to longitudinal and lateral slip:

$$s_x = -\kappa = -\frac{V_{x,slip}}{V} = -\frac{V - V_r}{V} = -\frac{V - \omega \cdot R_e}{V}$$

$$s_y = -\tan(\alpha)$$

The deformations e_x and e_y (see [figure 2](#)) can be expressed mathematically in terms of slip, position in the contact area, tread stiffness, friction coefficient and pressure distribution. From these expressions, closed form expressions can be derived for the shear stress within the contact area. Integration over the contact area leads to expressions for lateral force, brake force, pneumatic trail and aligning torque in terms of slip.

These relationships are shown graphically in the figures below. In the first plot, the side force is shown versus slip angle for various values of brake slip (i.e. for combined slip). One observes that F_y reduces for increasing brake slip. In the plot below that one, the pneumatic trail is shown versus slip angle, where one observes that the pneumatic trail reduces to zero for increasing side slip and/or brake slip. This can be explained from the symmetrical deformation pattern for large slip (fully sliding of the tyre).

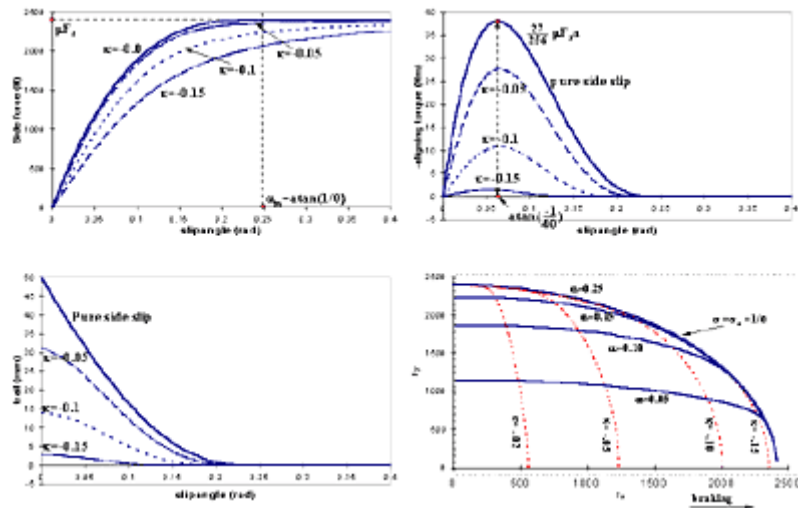


Figure 3 - Brush-model results

Pneumatic trail times side force leads to aligning torque (upper right). Finally, the fourth plot shows side force versus brake force for constant lateral slip (α) or brake slip (κ). Compare these figures with the figure 15 and figure 16 in chapter "Tyre-road friction and tyre slip". Some deficiencies are shown such as the lack of local maximum in the shear forces, and the lack of unsymmetry in the $F_x - F_y$ plot. These deficiencies can be corrected by improvement of the brush model:

- include carcass stiffness, see [figure 4](#) to the right where the tread deformation is connected to the original wheel symmetry plane through linear springs.
- introduce different tread stiffnesses in x- and y-direction
- take the friction coefficient dependent on sliding speed.

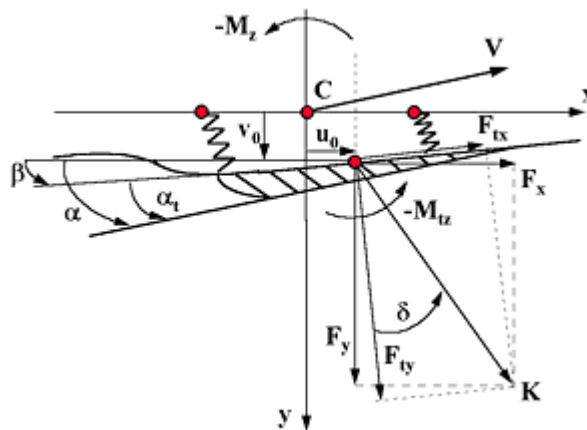


Figure 4 - Improved brush model, including carcass stiffness

The empirical Magic Formula model.

We have treated the bicycle model, being the simplest of its kind and most often used in the first attempts at developing vehicle design concepts. More in-depth analysis requires more complex models, for which special simulation packages are available such as ADAMS, DADS, SIMPACK, MADYMO.

The models employed use a description of tyre behaviour. A requirement for

specific vehicle behaviour, expressed in characteristic vehicle parameters, should produce insight into the desired tyre specifications that are given to the tyre manufacturer for this vehicle. That requires a manageable tyre model in which measurement data are translated sensibly into tyre properties.

Before 1980, such a kind of a model was not available. Things changed at that time, when professor Pacejka, in conjunction with Volvo, developed an empirical formula at the Delft University in which these properties could be described in closed form, the so-called Magic Formula (see [8.2]):

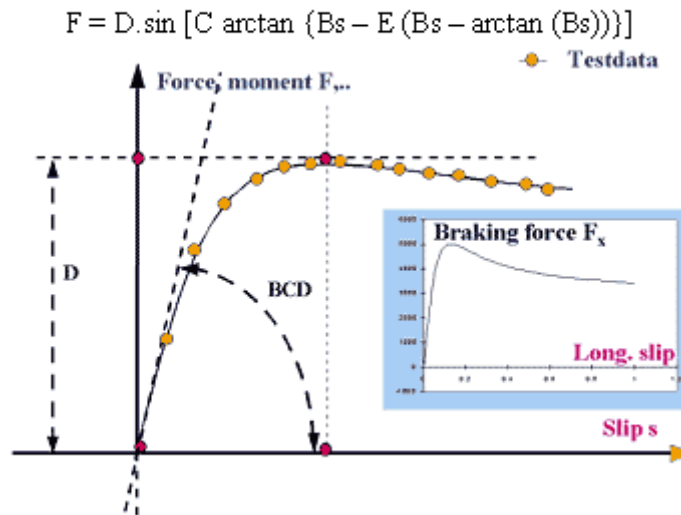


Figure 5 - The Magic Formula tyre model

F could be brake force or side force, and s the longitudinal or lateral slip. The shape of the curve is described by the coefficients B, C, D and E which once again depend on the wheel load and the camber angle. Taken together, a formula was now available to capture the complete stationary behaviour of a passenger car tyre in a limited number of parameters.

In a similar way, the pneumatic trail can be described by a Magic Formula with sine replaced by cosine.

Transient and dynamic behaviour

For quick variations in brake force, such as occurring for braking over uneven road surfaces, or in side force for wheel oscillations, the assumption of stationary tyre behaviour no longer suffices. The tyre's belt can in the first instance be considered as an elastically reinforced stretched string, see [8.1], [8.3].

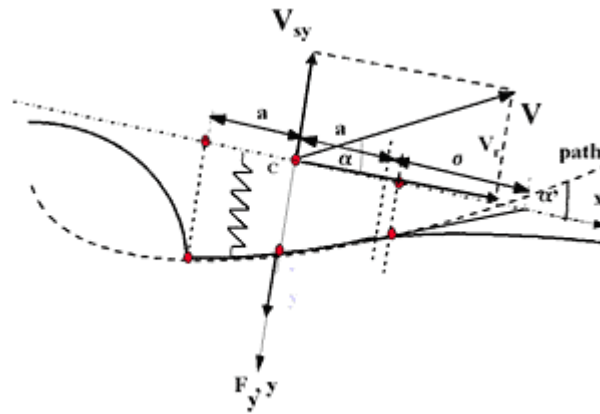


Figure 6 - Transient tyre behaviour

For quick variations to tyre force, the tyre needs time to attain the stationary response. The distance over which 63% of the stationary deflection is realised is indicated by the relaxation length σ . Accounting for lateral displacement $y(t)$ of the tyrebelt in contact with the road, the actual slip angle α' can be described by:

$$\alpha' = \alpha - \frac{dy}{dt} \cdot \frac{1}{V_r}$$

Combining with (assuming small slip angle):

$$F_y = C_{cy} \cdot y = C_{F\alpha} \cdot \alpha'$$

lateral tyre stiffness C_{cy} and cornering stiffness $C_{F\alpha}$ one arrives at the first order system:

$$\sigma \cdot \frac{dF_y}{dt} + V_r \cdot F_y = V_r \cdot C_{F\alpha} \cdot \alpha$$

for σ defined as the ratio of the cornering stiffness and the tyre lateral stiffness. Using the linear relationship between side force and slip angle, this equation transforms into:

$$\frac{1}{V} \cdot \frac{dv_1}{dt} + \frac{v_1}{\sigma} = \tan \alpha$$

For faster excitations, oscillations in the belt can occur in addition to the delay behaviour already mentioned, with a movement of the belt as a whole in relation to the rim as the oscillation mode at the lowest frequency, see [8.4]. The belt takes on a life of its own as it were. This situation is mainly relevant for passenger and light-truck tyres in the discussion of durability, ride comfort and alike.

A schematic picture of the tyre model used to describe such excitations is shown below.

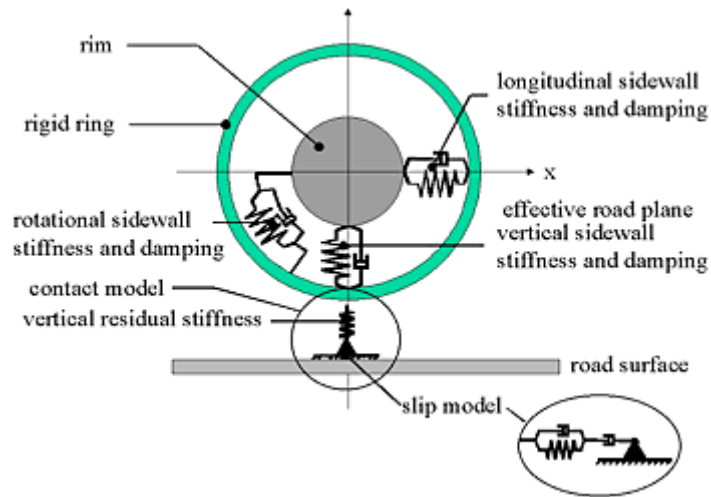


Figure 7 - In-plane dynamic tyre model

For several tyre models, the response of the passenger tyre to a step and a trapezoidal obstacle have been determined, in terms of vertical and longitudinal force at the wheel axle. Clearly, when the belt starts to oscillate around the rim, one expects these oscillations to be apparent in the $F_z(t)$ and $F_x(t)$ plot. Results are shown below. One observes two different frequencies, where the lower one (especially seen in the $F_x(t)$ plot) corresponds to the eigenmotion of the belt, moving horizontally (pivoting around the contactpoint) in phase with the rim-motion.

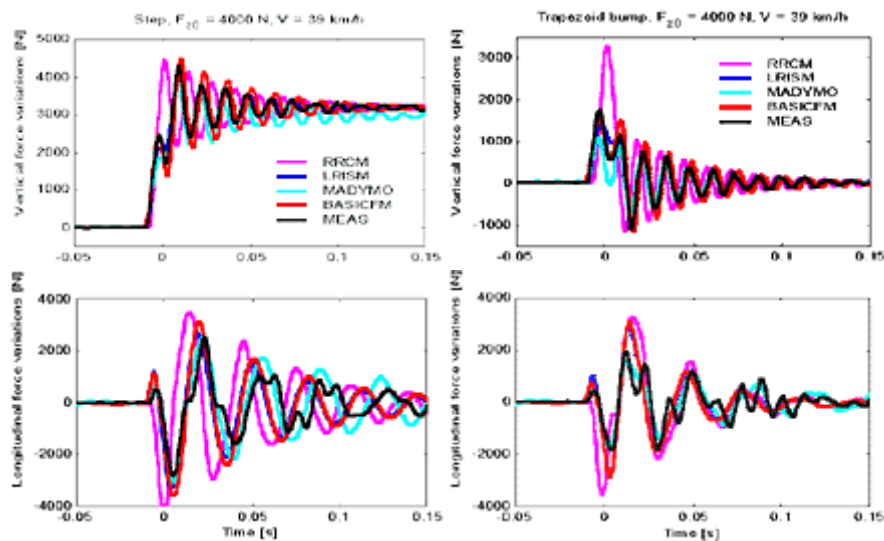


Figure 8 (a, b, c, d) - Dynamic tyre performance, rolling over a single step

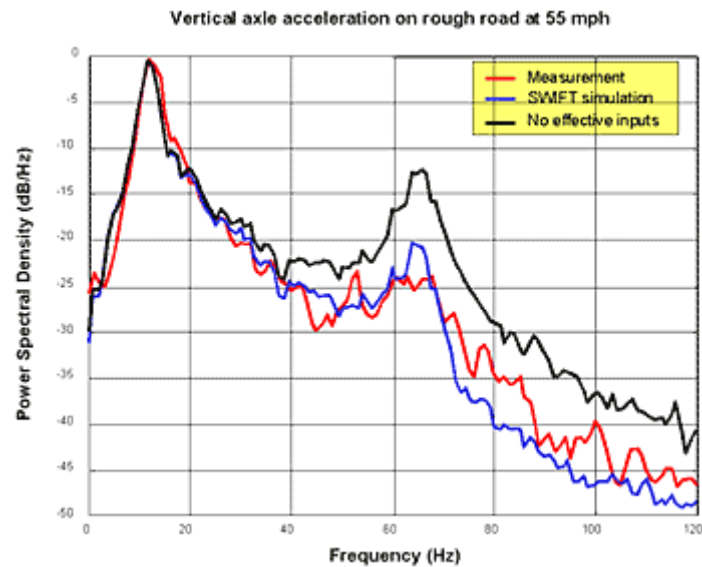


Figure 9 - Light-truck ride performance and dynamic tyre behaviour

The research on these efficient rigid belt tyre models has results in the derivation of the SWIFT-TYRE software tool. Some comparison of ride-comfort frequency output for a light-truck tyre, obtained experimentally and using the SWIFT tyre model, is shown below, with and without taking account of the tyre enveloping properties. One observes that these enveloping properties (described by SWIFT as well) cannot be neglected beyond 20 Hz. Even up to high frequency, an excellent match is obtained between simulation and experiment.

Measurement of truck tyre slip characteristics

In this section, some recent test results will be discussed, a major part of which have been derived as part of a large SAE-project, see [9.1] - [9.4].

Before going in detail about these results, let's sum up some of the possible facilities that can be used for tyre testing, most of which are available in Delft at TNO-Automotive and the Delft University of Technology.

Tyre experiments can be carried out on the road and in the laboratory. In addition, one might be interested in steady state tyre data or dynamic tyre data such as relaxation length, side-wall stiffness and damping properties, etc.

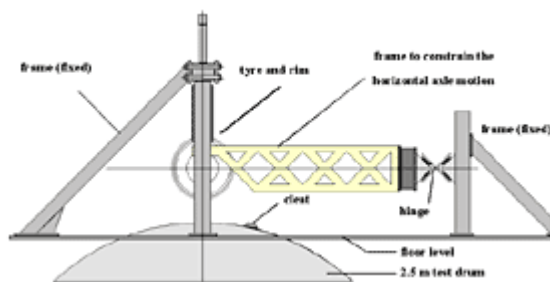
The following facilities as available in Delft:

- High-speed drum test benches:
 - Cleat and brake test stand
 - Pendulum test stand
 - Yaw oscillation test stand
 - Tire measurement tower

- Flat-plank test bench:
 - Enveloping properties
 - Parking manovres
- Out-door:
 - Delft-tyre Test Trailer

Delft-tyre Test Trailer

The DELFT-TYRE Test Trailer is equipped for steady state tyre testing under pure cornering, pure braking and combined cornering and braking conditions, enabling tyre testing of a tyre mounted on a vehicle under real life conditions.



Cleat and brake test stand.

This facility is used for studying the in-plane dynamic performance of the tire under brake torque variations as well as under the loading by specific road disturbances in the frequency range 0 - 100 Hz. The tire is mounted on top of the drum with constrained vertical and horizontal axle motions.

The vertical axle height can be adjusted to load the tire on the drum. The variation in reaction forces of the tire are measured at both wheel bearings with Piezo electric elements. To ensure that a pure brake torque is applied to the wheel axle, the brake system is mounted on a separate structure. Brake shaft and wheel shaft are connected with an intermediate shaft through two flexible couplings (flexible in all directions except about the axis of revolution). Applied brake torque is measured with strain gauges in the coupling shaft.

Wheel slip is determined from wheel and drum angular velocity. Brake pressure is controlled by a hydraulic servo system with the desired brake pressure signal generated by a separate processor, allowing arbitrary selection of various kind of excitations: sinusoidal, block, successive steps, random variations or sinusoidal sweeps.

The test stand has also been used for experiments to determine the effective input as well as to validate these under dynamic conditions, with different obstacle shapes.

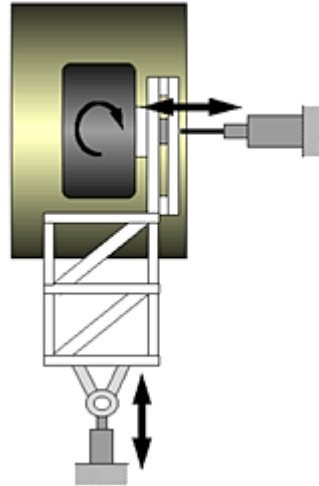
Recently, this facility has been renewed to allow tests with light-truck tyres and race tyres as well. In addition, a special acoustic cover was established for the high-speed drum (also to ensure better confidentiality).



Pendulum test stand.

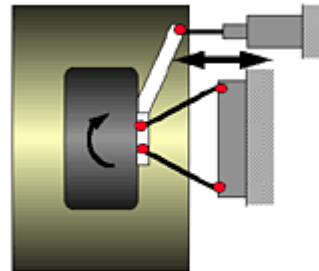
The pendulum test stand consists of a stiff frame (pendulum arm) which can rotate about a vertical hinge. A measuring hub with the wheel axle is mounted on a special steering head at the free end of the pendulum arm. This steeringhead is used to adjust the average tire slip angle (between -3° and 8°). A small hydraulic

cylinder at some distance above the wheel axle level, is used to apply the vertical load on the tire. The force variations are measured with the hub containing piezo-electric force transducers from which the total lateral force, the aligning moment and the overturning moment can be calculated.



Yaw oscillation test stand.

The yaw test stand includes a trapezoid with flexible hinges at the corners. The two rigid beams in this trapezoid connect the measuring hub to a frame, rigidly connected to the floor foundation. The design is such that centre point steering is guaranteed, i.e. the steering axis passes through the centre of the tire contact patch. The displacement of a hydraulic cylinder is transformed into a wheel rotation through a rigid excitation arm, mounted to the measuring hub. The tire load is applied by adjusting and fixing the axle height.



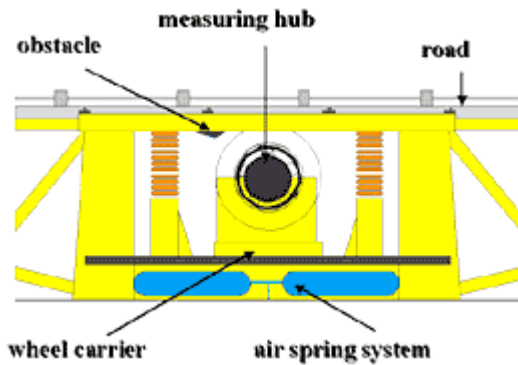
Measurement tower.

The measurement tower was designed to carry out in-door combined slip measurements and vertical compliance testing. Tire and measuring hub can be moved vertically, controlled with a hydraulic cylinder. The entire rig can rotate about the vertical axle, with the steering angle adjusted by another hydraulic cylinder.



The same hydraulic servo system as used in the separate cleat and brake test

stand is used here to control the brake pressure. Wheel and drum angular velocities are obtained also similarly to this cleat and brake test stand. Forces are measured at the wheel bearings using strain gauges. The maximum frequency for operating this test stand amounts approximately 20 Hz.



Flat plank tyre test bench.

This bench is designed to derive low speed tyre characteristics, such as parking performance on different surfaces and enveloping properties (essential for dynamic tyre modelling) for different type of road disturbances. Experiments can be carried out for fixed axle height or fixed axle load. Speed varies between 1 and 45 mm/s.

The results of [9.1 - 9.4] are discussed only briefly. It is recommended to further consult the references.

This SAE cooperative research had the following objectives:

- To understand truck tyre behaviour
- To derive a standardised test procedure for:
 - free rolling cornering
 - straight line braking
 - combined slip
- To compare in-door / out-door tests
- To investigate the influence of wear, speed, pressure, water depth
- to obtain data for 295/75R22.5 truck tyres (ribbed steer, lug drive axle)

Tests were carried out for these tyres on the CALSPAN flat-belt facility and with the UMTRI Mobile Test Trailer, with the following specifications:

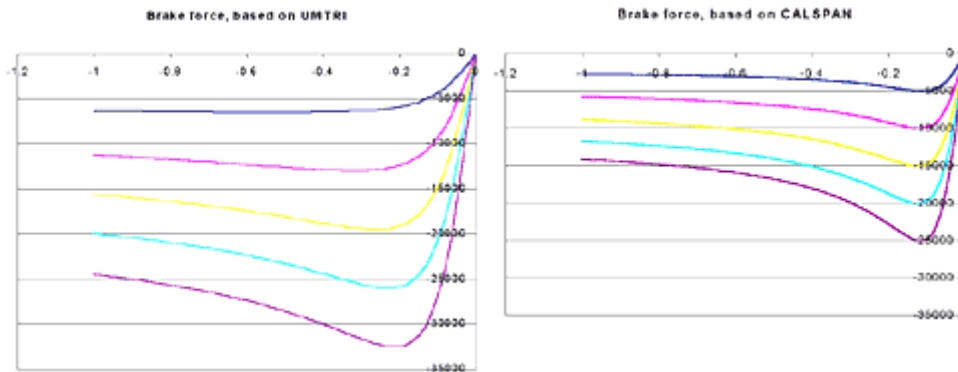
- | | |
|----------------------------------------------------------------------------------------------------------------------------------------------------------------------------------------------------------------------------------------------------------------------------------------------------------------------------------------------------------------------------------------------------------------------------------------------------------------------------------|--------------------------------------------------------------------------------------------------------------------------------------------------------------------------------------------------------------------------------------------------------------------------------------------------------------------------------------------------------------------------------------------------------------------------------------------------------------------------------------------------------------------------------------------------------------------------------|
| <ul style="list-style-type: none"> • CALSPAN TIRF • Indoor steel belt • Temperature effects • Sand paper coating • Flat surface belt • dry road conditions • $V < 320$ km/hr • $F_x < 33400$ N • $F_z < 54000$ N • Dynamics ?? • Tyre diameter < 47 inch • Tread width < 24 inch | <ul style="list-style-type: none"> • UMTRI Mobile test trailer • On the road • Semitrailer, towed by instrumented tractor • Trailer station: braking • Tractor station: combined • wet conditions • $V < 96.5$ km/hr • F_x (slowing down?) • $F_z < 106700$ N • No dynamics • Tyre diameter < 54 inch • Braking: $r_e < 19$ inch • Tread width < 19 inch |
|----------------------------------------------------------------------------------------------------------------------------------------------------------------------------------------------------------------------------------------------------------------------------------------------------------------------------------------------------------------------------------------------------------------------------------------------------------------------------------|--------------------------------------------------------------------------------------------------------------------------------------------------------------------------------------------------------------------------------------------------------------------------------------------------------------------------------------------------------------------------------------------------------------------------------------------------------------------------------------------------------------------------------------------------------------------------------|

Amongst others, the following observations were made.

Brake tests.

A strong difference between test results for both facilities were apparent. These difference appeared in the peak values (differences in the order of 25 %), the brake slip for which this peak was obtained (varying between 10 and 20 %), and the behaviour beyond this peak value. There is an important surface friction effect.

We have estimated these curves for both facilities using the Magic Formula to indicate these differences, see figures below.



Cornering tests

Good correspondence between both facilities, with slip angles up to about 8 degrees. The lateral force peak value wasn't reached.

External influences and service conditions.

Treadwear has a large impact on the lateral force, in contrast to the longitudinal force.

There is an effect of speed on dry pavement. Different shapes for combined slip for different speeds were reported, with slip ratio's approaching sliding

The combined effect of wear, water depth and speed have strong effect on traction forces, especially with low loads. The change of aligning moment as a function of wear, water depth, speed can be complex.

As an overall conclusion one can say that the project starts to give us an understanding in assessment of truck tyre data and its reliability, accounting for various external conditions that might effect the testresults. In this way, this project is a very valuable contribution in truck tyre research. Nevertheless, a correlation between truck-tyre test results with different facilities under such severe conditions such as sweep in the slip angle and (combined) brake test is hardly obtained. The pure lateral slip measurements give reasonable good results, but as soon as braking is applied, the resemblance is lost.

References

[1.1]. French, T., Tyre Technology, Ed. Adam Hilger, Bristol, 1989.

[1.2]. Dixon, J.C., Tyres, Suspension and Handling, Cambridge University Press, Cambridge, 1991.

[1.3]. Schuring, D.J., Scale Modeling of Equilibrium Tire Temperature, Tire Science and Technology, TSTCA, vol.1, no.3, 1973.

[1.4]. Bueche, F., Physical Properties of Polymers, Interscience Publishers, New York, 1962.

[2.1]. Ford, T.L. and Charles, F.S., Heavy Duty Truck Tire Engineering, SAE Paper no. 880001, 1988.

[2.2]. Seitz, N. and Hussmann, A.W., Forces and Displacement in Contact Area of Free Rolling Tires, SAE Paper no. 710626, 1971.

[2.3]. Browne, A., Ludema, K.C. and Clark, S.K., Contact Between the Tire and Roadway, in Mechanics of Pneumatic Tires, Ed. S.K. Clark, U.S. Department of Transportation, N.H.T.S.A., Washington D. C., 1981.

[3.1]. Göhring, E., Von Glasner, E.C. and Pflug, H.C., Contribution to the Force Transmission Behavior of Commercial Vehicle Tires, SAE Paper no. 912692. 1991.

[5.1] J.C. Dixon.: Tires, Suspension and Handling. SAE International, Arnold, a member of the Hodder Headline Group, London (1996).

[5.2] J.R. Ellis: Vehicle Handling Dynamics, Mechanical Engineering Publications (1994)

[5.3] Th. D. Gillespie: Fundamentals of Vehicle Dynamics, Society of Automotive Engineers (1992).

[5.4] D.J. Bickerstaff.: The Handling Properties of Light Trucks. SAE 760710

[5.5] H.B. Pacejka.: Simplified behaviour of steady state turning behaviour of motor vehicles, part 1: Handling diagrams and simple systems. Vehicle System Dynamics 2, 1973, pp. 162 - 172.

[5.6] H.B. Pacejka.: Simplified behaviour of steady state turning behaviour of motor vehicles, part 2: Stability of the steady state turn. Vehicle System Dynamics 2, 1973, pp. 173 - 183.

[5.7] H.B. Pacejka.: Simplified behaviour of steady state turning behaviour of motor vehicles, part 3: More elaborate systems. Vehicle System Dynamics 2, 1973, pp. 184 - 204.

[5.8] C.B. Winkler.: Simplified Analysis of the Steady-State Turning of Complex Vehicles. Vehicle System Dynamics, 29 (1998), pp. 141 - 180

[6.1]. H.B. Pacejka.: Handling and Stability of Commercial Vehicles. DAF Lecture, 1983.

[7.1]. R.D. Ervin, C. Mallikarjunarao.: A study of the yaw stability of tractor -

semitrailer combinations, Proceedings IAVSD, p.111, Swets & Zeitlinger BV-Lisse (1982).

[7.2]. J.P. PAUWELUSSEN: Analysis and prevention of excessive lateral behaviour of articulated vehicles. XII International Heavy Truck Conference, 13-15 September 1995, Budapest, Hungary

[7.3]. J.P.PAUWELUSSEN.: Excessive yaw behaviour of commercial vehicles, a fundamental approach. To be presented at: Enhanced Safety of Vehicles (ESV) 2001.

[8.1]. Pacejka, H.B.: The Role of Tyre Dynamic Properties. In.: Pauwelussen, J.P, Pacejka, H.B.: Smart Vehicles. Swets & Zeitlinger, Lisse, The Netherlands (1995).

[8.2]. Pacejka, H.B.: The Tyre as a Vehicle Component. Proceedings of the XXVI Fisita Congress, Prague, Czech Republic (1996)

[8.3]. Pacejka, H.B., Besseling, I.: Magic Formula Tyre Model with Transient Properties. 2nd International Tyre Colloquium on Tyre Models for Vehicle Dynamic Analysis, Berlin, Germany (1997). Swets and Zeitlinger.

[8.4]. A. Schmeitz, J.P. Pauwelussen: High Frequency Tyre Response for Arbitrary Road Input. Haus der Technik, Essen, June 2000

[9.1]. M.G. Pottinger, W. Pelz, G.A. Tapia, C.B. Winkler.: A free rolling Cornering Test for Heavy-Duty Truck Tires. Presented at the Tire Society Meeting, 1995. Tire Science and Technology (1995)

[9.2]. M.G. Pottinger, G.A. Tapia, C.B. Winkler, W. Pelz.: A Straight Line Braking test for Truck Tires. Rubber World 1996.

[9.3]. M.G. Pottinger, W. Pelz, G.A. Tapia, C.B. Winkler.: Truck Tires, 4th International Symposium on Heavy Vehicle Weights and Dimensions, University of Michigan, 1995.

[9.4]. M.G. Pottinger, W. Pelz, D.M. Pottinger, C.B. Winkler.: Truck Tire Wet Traction: Effects of Water Depth, Tread Depth, Inflation, and Load.: SAE 962153.